Metrics and Statistical Modeling of Ambient Noise with Emphasis on Calving Noise from a West Greenland Fjord

Dara Farrell

A dissertation
submitted in partial fulfillment of the
requirements for the degree of

Doctor of Philosophy

University of Washington

2019

Reading Committee:

Peter H. Dahl, Chair

Brian Polagye

Kevin Williams

Program Authorized to Offer Degree:
Mechanical Engineering

University of Washington

Abstract

Metrics and Statistical Modeling of Ambient Noise
with Emphasis on Calving Noise from a West Greenland Fjord

Dara Farrell

Chair of the Supervisory Committee:
Dr. Peter H. Dahl
Mechanical Engineering, Applied Physics Lab

This dissertation is a compilation of explorations of various methods related to mapping, methods and modeling. These methods are useful in the study of acoustic data. The exploration of data in this work from a Greenland fjord represents most (although not all) of these methods and therefore influences the title of this work.

In this work, the background noise environment in a glacial fjord was measured and the data were analyzed. The work explores the utility of spectral probability density (SPD) in evaluating background noise characteristics in the frequency domain, models probability density functions (PDFs) of spectral levels and introduces a parameter σ_T that quantifies the character of noise in frequency bands of interest; this work demonstrates that the empirical PDFs used in the SPD can be replaced by analytical PDFs if the spectral estimates can be considered to be exponential random variables. It also explores the utility of k-medoids clustering as a pre-sorting method to inform the selection of features on which to base the training of more complex algorithms.

TABLE OF CONTENTS

LIST OF FIGURES

LIST OF TABLES

ACKNOWLEDGMENTS

The author wishes to express sincere appreciation to the members of her committee and family and friends, the department of Mechanical Engineering and the University of Washington, where she has had the opportunity to learn and grow.

DEDICATION

to my family and friends who have helped me to get this far

Chapter 1

INTRODUCTION

This dissertation comprises three chapters bracketed by this introductory chapter and a concluding chapter presenting final remarks. The three chapters that form the body of this work represent a compilation of my exploration of various methods related to mapping, metrics and modeling that I have found useful in the study of acoustic data. However, the exploration of data from a Greenland fjord represents most (although not all) of these methods, and therefore influences the title of this work.

Chapter 2 is a tutorial chapter on the use of Geopgraphic Information System (GIS) tools in the context of underwater noise modeling, documenting past work in the use of GIS for mapping zones of influence related to pile driving noise. Although no true spatial analysis is undertaken in this dissertation, this tutorial outlines the foundation for visualizing transmission loss maps and creating layers that can be integrated with other spatial data.

Chapter 3 discusses the use of metrics in the study of ambient noise levels for the 2013 Target and Reverberation Experiment and is an example of the application of spectral probability density (SPD) for quantifying background noise levels, a tool which is also used in later work. This chapter was previously published in the IEEE Journal of Oceanic Engineering in October 2017 [14]. It presents an analysis of the time and frequency domain properties of a multi-day series of background noise during the Target and REverberation eXperiment (TREX13) that took place off the coast of Panama City, FL, USA. Background noise was measured at two locations separated by approximately 1 km in waters of depth approximately 20 m. The two locations were south-east of the moorage location of the *R/V Sharp* [30° 3.59' N, 85° 40.83' W], from which monostatic reverberation studies were conducted.

The median spectral density level estimated for a frequency band centered at 2.7 kHz with a bandwidth of 1800 Hz was comparable to the median level at 3.5 kHz averaged over a bandwidth of 100 Hz; both were estimated to be 60 dB re 1 μ Pa^2/Hz when averaged during the day or night. In contrast, the level at 4.5 kHz, estimated by averaging over a bandwidth of 100 Hz, increased by 14 dB at night. While the data suggest a degree of consistency in the background environment for the purposes of modeling, when assessing levels in the 80 to 8000 Hz frequency band time of day was found to be influential. The median spectral levels presented may be used to assess the influence of background noise at a given time of day. Biological noise likely from fish was revealed to be a significant contributor to background noise at night, and daytime background noise levels were primarily influenced by wind.

Chapter 4 discusses the analysis of underwater acoustic data collected in a west Greenland fjord. The chapter discusses background noise trends and the detection of events in the fjord with an emphasis on metrics and statistical modeling. Predicting future sea levels depends on accurately estimating the rate at which ice sheets deliver fresh water and ice to the oceans and projecting rates of iceberg calving will be improved with more observations of calving events. This chapter includes an analysis of methods useful for evaluating background noise. It explores the utility of spectral probability density in evaluating background noise characteristics in the frequency domain, models probability density functions of spectral levels and introduces a parameter σ_T that quantifies the character of noise in frequency bands of interest. This work demonstrates that the empirical PDFs used in the SPD can be replaced by analytical PDFs if the spectral estimates can be considered to be exponential random variables. It also explores the utility of k-medoids clustering as a pre-sorting method to inform the selection of features on which to base the training of more complex algorithms.

Chapter 5 summarizes the previous chapters and presents some concluding remarks.

Chapter 2

MAPPING FOR DECISION MAKING: GEOGRAPHIC INFORMATION SYSTEM APPROACHES RELEVANT TO UNDERWATER NOISE MAPPING.

2.1 Introduction

It has been widely acknowledged that human activity affects the natural environment. The high levels of underwater noise from anthropogenic activities, such as pile driving, may endanger and cause changes in the behavioral patterns of marine mammals and fish [18,33]. Therefore, the visualization of the spatial extent of the underwater noise field produced by these activities is helpful for both regulators as well as operators.

Marine construction activities require applications for incidental harassment authorization (IHAs) for shorter periods of activity, or Letters of Authorization (LOAs) for longer periods of activity since these activities are subject to stipulations within the Endangered Species Act (ESA), the Marine Mammal Protection Act (MMPA) and National Environmental Policy Act (NEPA). Within these IHAs and LOAs are stipulated levels that delineate zones of influence (ZOIs) for physiological damage and behavioral impacts (disturbance) to marine life. Government agencies in Washington State expend a significant amount of human and monetary resources to comply with requirements contained within IHAs and LOAs. These agencies include the Washington State Dept. of Transportation (WSDOT), Washington Department of Fish and Wildlife, the U.S. Fish and Wildlife Service, and the National Marine Fisheries Service, to name but a few.

Decisions on the deployment of monitoring personnel during marine construction activities increasingly require a spatial understanding of the extent of these zones of influence. Overly-conservative delineation of monitoring zones can result in higher labor costs and over-

all costs of the monitoring effort. This chapter outlines the use of GIS in visualization of a particular model of transmission loss (TL) for particular locations on the east coast where impact and vibratory pile driving operations were being planned.

GIS offers a platform for organizing and assembling databases relevant to underwater noise monitoring and facilitates spatial analyses and map rendering, which can offer a powerful visual tools for supporting the decision-making process. While there are several widely used GIS software packages such as ArcGIS, QGIS, and GRASS, this tutorial employs the use of terms applicable to the ArcGIS suite of tools in describing a procedure for producing these transmission loss maps. However the methods discussed here can be readily generalized to visualizing other transmission loss models using other software packages. Where necessary it may be helpful to refer to a glossary of GIS terminology [29] to provide additional context for the following section.

2.2 Phases of the GIS Project: case study of underwater noise mapping

The application of GIS for decision support in underwater noise mapping will be discussed in the following phases, which are part of an iterative process (Figure 2.1): identifying project objectives, formulating specifications, developing the analytical framework, locating data sources, organizing and manipulating data for input, analyzing data and verifying outcomes, and evaluating output. This section outlines a practical implementation of these seven phases in the creation of acoustic transmission loss maps that help visualize the decay of sound level with range. As an example we show some samples for a case involving marine pile driving at a naval facility near Norfolk, VA. The samples originate from a project that the UW Applied Physics Laboratory was engaged in on behalf of the Naval Facilities Engineering Command (NAVFAC).

2.2.1 Identifying project objectives

The first phase consists of conceptualizing the problem to be addressed with GIS. The articulation of clear objectives and project goals will have bearing on the ultimate utility of

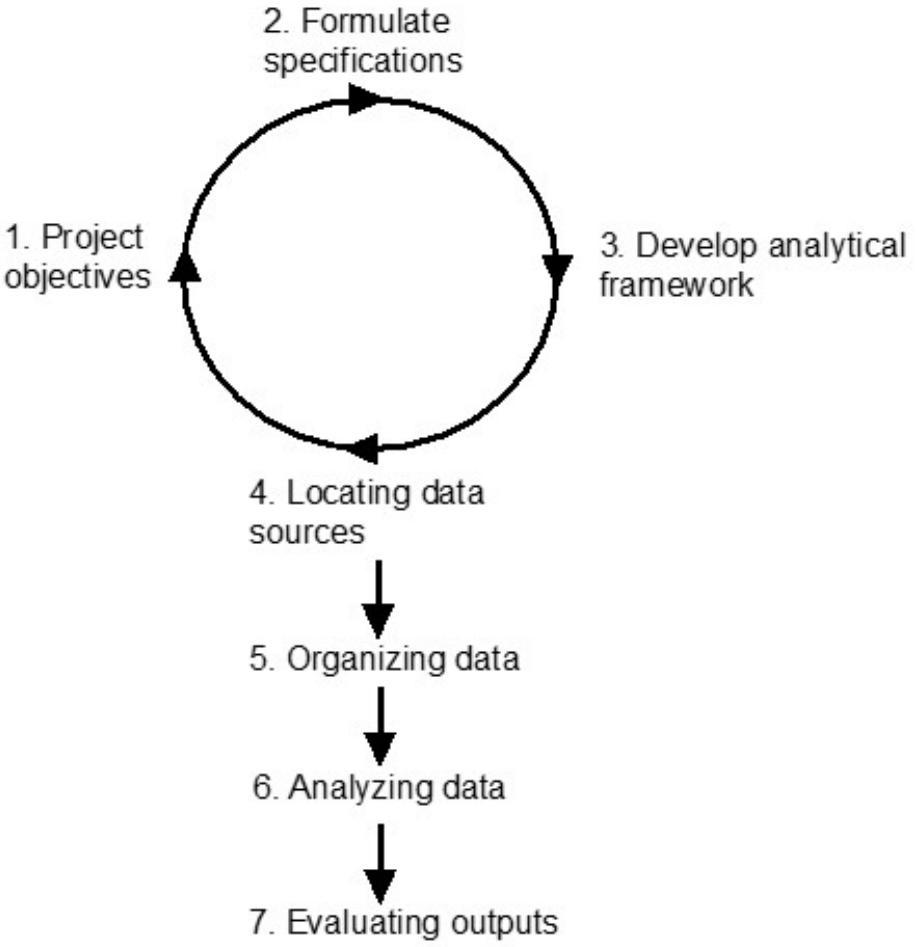

Figure 2.1: Phases in the application of GIS for decision making (adapted from [27])

the analysis, and therefore requires active participation and close involvement of all stakeholders. In the case study objectives were outlined in consultation with the stakeholders for this project (an environmental consulting company and NAVFAC) locations were selected for modeling of transmission loss. This is a critical step; carefully articulating the decision to be supported by GIS can yield time and cost savings by avoiding preparation of data layers that may go unused.

2.2.2 Formulating specifications

Once an overall understanding of project objectives has been developed, it may be helpful to develop a list of more functional specifications related to each objective which may include (but not be limited to) required projects, metadata standards, and accuracy requirements. Specifications for the final GIS product were outlined in the statement of work and included specification of the preferred map projection and metadata standards. The final product was required to be a raster file projected in the Universal Transverse Mercator (UTM) coordinate system, using the zone appropriate to the project area and using meters as the standard unit of measurement.

2.2.3 Developing the analytical framework

Development of the analytical framework primarily concerns how project objectives identified in earlier steps will be met. In the context of underwater noise mapping, this phase entails deciding on the type of underwater noise model to employ. This choice, for example, may depend on the type of marine construction noise to be evaluated, such as impact pile driving, vibratory pile driving, drilling, etc. Additionally, for the purposes of mapping the final results of the acoustic modeling must be expressed as function of location or range, i.e., depth information is typically averaged out. Several methods acoustic modeling are available, e.g, range-independent approaches where bathymetry is fixed and other conditions such as sound speed are sediment characteristics are a function of depth [24], or approaches that incorporate range dependence [11]. Since details on specific acoustic models are not essential for the discussion of this chapter these will not be discussed further, although we comment briefly on some key features of underwater acoustic propagation as it applies to spatial mapping.

2.2.4 Locating data sources

After an analytical framework has been developed, it is necessary to identify the data needed for the overall analysis [27]. If data required for the analysis are lacking, project objectives

should be revised or reevaluated altogether. In general, the collection of primary (field) data can be costly and time consuming. Instead, data are usually acquired through a variety of secondary sources such as local, state and federal geospatial clearinghouses. Common challenges faced in locating data sources generally involve data availability (some data that might be useful simply have not been collected and aggregated for spatial representation, may not be publicly available, or may not be available at sufficient resolution), accuracy (occasionally databases and layers that do exist have errors/inaccuracies and these errors can skew analyses), and standardization (data layers maintained by different agencies or bodies may for example be projected in different coordinate systems).

In the current case study, NAVFAC provided bathymetric surveys for the required locations as textfiles and GIS shapefiles. Sediment composition data were obtained from the usSeabed database [40] and proprietary dredge sample sediment data for limited locations were combined to allow a broad classification of sediment type for each site as either sand or mud. This was based on the prevailing sediment type within 2000 m of the pile driving modeling locations.

The sound speed in the water column was assumed to be constant for all sites with seasonal dependence. Seasonal temperature and salinity values were used to calculate the water sound speed using the Chen Millero algorithm [4], whereas the sediment sound speed was kept constant for both summer and winter. We justify this approximation on the basis of [46], where it is noted that temperature gradients in the sediments may usually be ignored. The result is an important effect as illustrated in Figure 2.2, where owing to the higher constrast in water versus sediment sound speed in winter conditions, the critical angle increases. This has the effect of improving the conditions for the propagation of underwater sound that ultimately can influence the ZOI.

2.2.5 Organizing and manipulating data

Once the data have been identified and collected, they should be organized into a database for use in the target GIS [27]. This phase includes verification of data quality, data consolidation

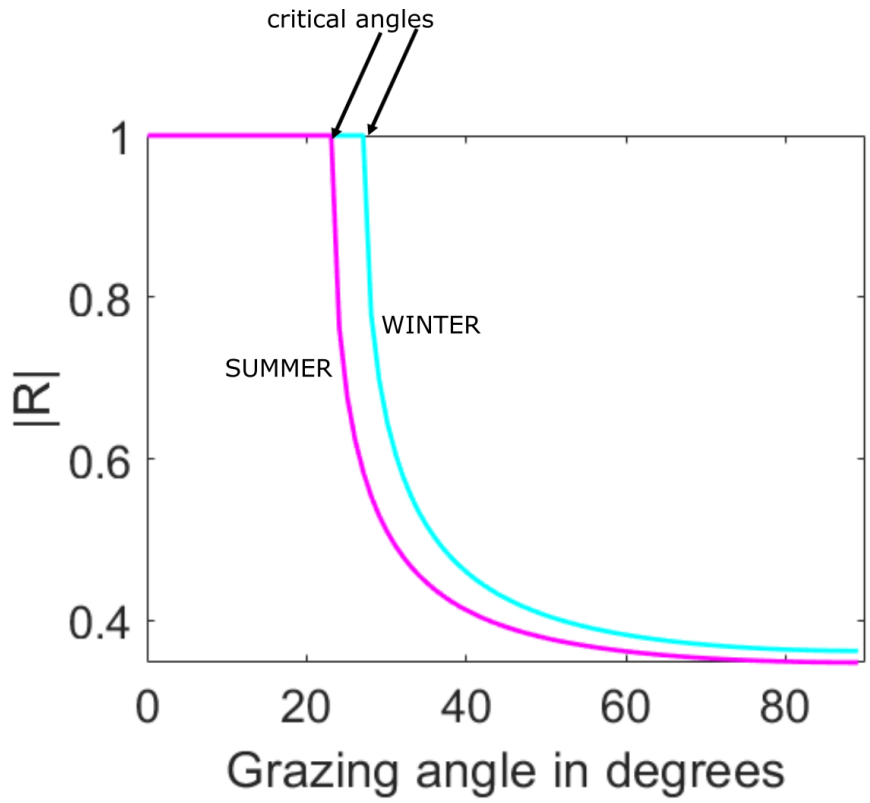

Figure 2.2: Magnitude of the plane wave reflection coefficient —R— as a function of grazing angle for summer and winter conditions as applied to acoustic modeling in the Norfolk area. The sediment sound speed is assumed to be 1650 m/s and the water speed is taken as 1516 m/s (summer) and 1416 m/s (winter), resulting in a higher critical angle for winter conditions.

and reformatting, and, in some cases, creation of derived data layers. Interpolation methods may be required to derive continuous spatial layers from point data obtained at discrete locations.

In the current case, the provided naval survey bathymetry for some locations differed in the vertical datum (one location was referenced to the NAVD88 datum, while others were referenced to mean lower low water (MLLW)); an additional field was created for MLLW for the location referenced to NAVD88, which amounted to an adjustment of approximately 1.56 feet. Bathymetry was also sourced from the National Oceanic and Atmospheric Administration (NOAA). This was converted to points, and projected from geographic coordinates to stateplane coordinates. Bathymetry from these sources were combined; in the final raster preference was given to the more accurate naval surveys where appropriate. The ESRI terrain implementation of a TIN (triangular irregular network) was used to build a surface from the points. This terrain was converted to a raster of 10-foot cell size. In the final bathymetric raster, depths were converted from MLLW (in feet) to the mean sea level (in meters) required by subsequent processing and were interpolated so that the intervals were exactly 10 meters. A custom Python script was utilized in conjunction with the ModelBuilder tool within ArcMap to automate the creation of lines emanating from study locations. These lines were interpolated using the generated bathymetric raster to create a field that included depth (in meters). The lines, now called transects, could then be utilized for acoustic modeling.

The acoustic modeling was performed by others at the Applied Physics Laboratory and additional details are not essential to the scope of this chapter. From a GIS standpoint it was significant to note that the model required the following inputs: bathymetry, sediment sound speeds, and a regional and seasonal-dependent sound speed in the water column. Each TL estimate from the acoustic model was tied to the co-ordinates along each transect and was re-imported into ArcGIS as a new point shapefile with fields for X and Y co-ordinates as well as TL. The ESRI terrain implementation of a TIN (triangular irregular network) was used to build a surface from the points and visualize the model results.

2.2.6 Analyzing data

Ultimately the details of the analysis will be project specific, for example, dependent on the location of potential noise sources. Figure 2.3 shows season-dependent (summer and winter) model results. As indicted by Figure 2.3, conditions in summer and winter give rise to differences in the amount of acoustic energy that is transmitted or reflected. The higher water temperature in summer can produce greater TL because the sound speed contrast with the seabed is lessened and more acoustic energy is transmitted into the seabed. For reference the practical spreading model, which corresponds to TL = 15log10(Range/10) is also shown that does not take into account bathymetric changes and seasonal changes. The differences in the shapes of the transmission loss contours has implications for the sizes of the zones of influence for this location; the zones of influence are expected to be smaller in summer than in winter.

2.2.7 Evaluating outputs

The last phase involves evaluation of the outputs of the analysis and ideally should involve end-users, subject matter specialists, and the GIS analyst [27]. The final transmission loss maps were clipped to digitized shorelines and final phase involved checking that the finished product was adequately clipped to the shore in key areas. Upon final consultation with the stakeholders, the metadata for the shapefiles was formatted according to the required standard and the project was completed. It is common that final activities may include more detailed examination of individual components of the project together with any potential estimates of uncertainty or underlying assumptions. It is expected that initial project objectives should be compared to the outputs and updated, and the seven-step procedure re-initiated if necessary.

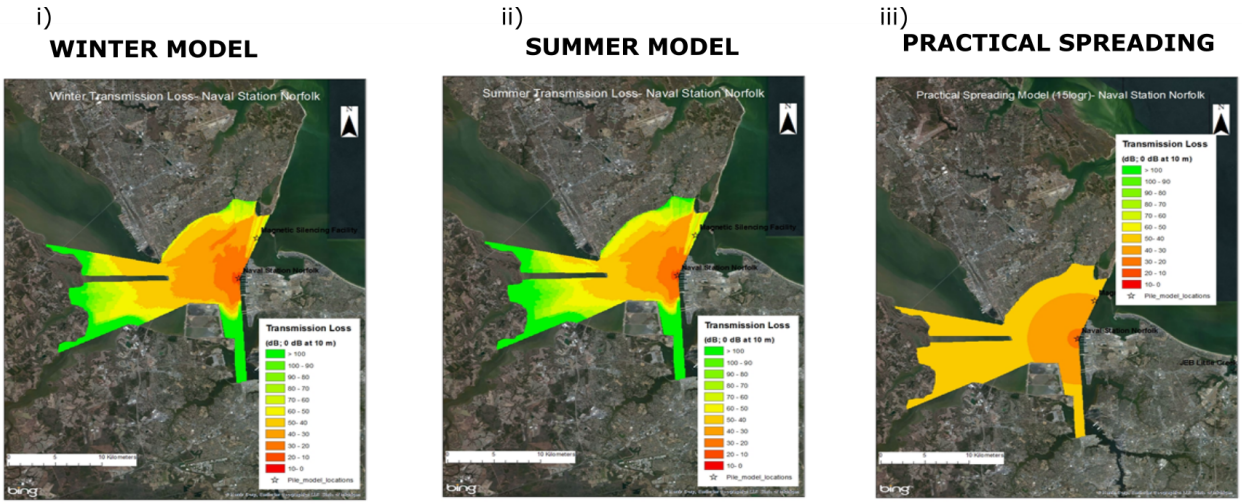

Figure 2.3: Transmission loss (TL) maps for a location in Norfolk, USA for winter (i) and summer (ii) conditions where bathymetry and seasonal changes in water column sound speed were included in modeling, compared with a model corresponding to TL = 15log10(Range/10) (iii) that does not take into account bathymetric changes and seasonal changes. These maps illustrate the effect of the warmer waters in summer, which produce greater TL.

2.3 Final remarks

Geographic information systems (GIS) offer an important framework for organizing spatial databases and performing spatial analyses. Here, we provided a brief overview of the utilization of GIS in the mapping of transmission loss using a location on the east coast of the United States. This section discussed the use of GIS in the mapping of underwater noise within the framework of phases of a GIS project. The maps produced demonstrated that bathymetry and time of year greatly influence the transmission loss map produced and hence the size of the zones of influence for a given location.

Chapter 3

METRICS: THE BACKGROUND NOISE ENVIRONMENT DURING THE 2013 TARGET AND REVERBERATION EXPERIMENT (TREX13)

3.1 Introduction

The 2013 Target and Reverberation Experiment, TREX13, took place from mid-April to mid-May of 2013. The main experimental goal was the measurement of reverberation in the mid-frequency range of 1-10 kHz, with an emphasis on the 2-4 kHz frequency band. These were combined with measurements of the sediment, water column and sea surface conditions at scales appropriate for modeling and interpretation of reverberation results. This chapter focuses on an analysis of the time and frequency domain properties of background noise within this band to support the overall science effort of TREX13. Some features of the background noise environment that cause variation within this band are also discussed such as biological sources (biophony) and wind activity (a component of geophony).

This chapter represents previously published work [14], and is arranged as follows: Section 3.2 describes the region where measurements were collected and includes a description of acoustic instrumentation. Section 3.3 discusses the noise time series observations and analyzes spectral density trends within experimental bands of interest; this section also discusses wind noise during a storm event that occurred during the deployment period of one of the acoustic recorders as well as significant sources of biological noise. Finally, Section 3.4 summarizes key emerging points.

3.2 Overview

3.2.1 Geographic Location and Bathymetry

The main experimental area was approximately 3.5 km offshore from Panama City, FL, where water depths ranged from 15 m to 25 m (Fig. 3.1). Two acoustic recording units were deployed approximately 1 m above the sea floor at 5 km [30° 1.9' N, 85° 38.4' W] and 6 km [30° 1.56' N, 85° 37.91' W] from the *R/V Sharp* where the reverberation source was located. The mean water depth at both locations was approximately 20 m.

3.2.2 Instrumentation

Acoustic data were collected in time series form using autonomous acoustic recorders (Digital Spectrogram Recorders, Loggerhead Instruments, Inc.). The 5 km and 6 km units were both equipped with hydrophones of nominal receive sensitivity -170 dB re 1 V/μPa and were set to continuously record over 4 and 19 day periods respectively. The units differed in sampling rates and system gain settings, with the lower sampling rate of the 6 km unit reflecting the limitations of available storage because of its longer deployment (Table 3.1). The gain response of the recording units is approximately flat over the frequency band considered in this analysis (80 Hz to 8000 Hz). We note that the cutoff frequency, f_c, for the first mode of this underwater environment is approximately 60 Hz based on the depth, $D = 20$ m, water sound speed, $c_1 = 1525$ m/s, and sediment sound speed, $c_2 = 1615$ m/s and using [21]

$$f_c = \frac{0.5 c_1 c_2}{2D\sqrt{c_2^2 - c_1^2}} \tag{3.1}$$

A comparison of data from the 5 and 6 km units over an overlapping 48-hour time period, April 27th 18:00 Z to April 29th 18:00 Z (Fig. 3.2), suggested a degree of consistency in the dominant background noise processes at each location. The relatively short time period of the comparison was motivated by the need to minimize periods of noise due to nearby boat traffic associated with the experiment at the 5 km unit as well as deployment and recovery

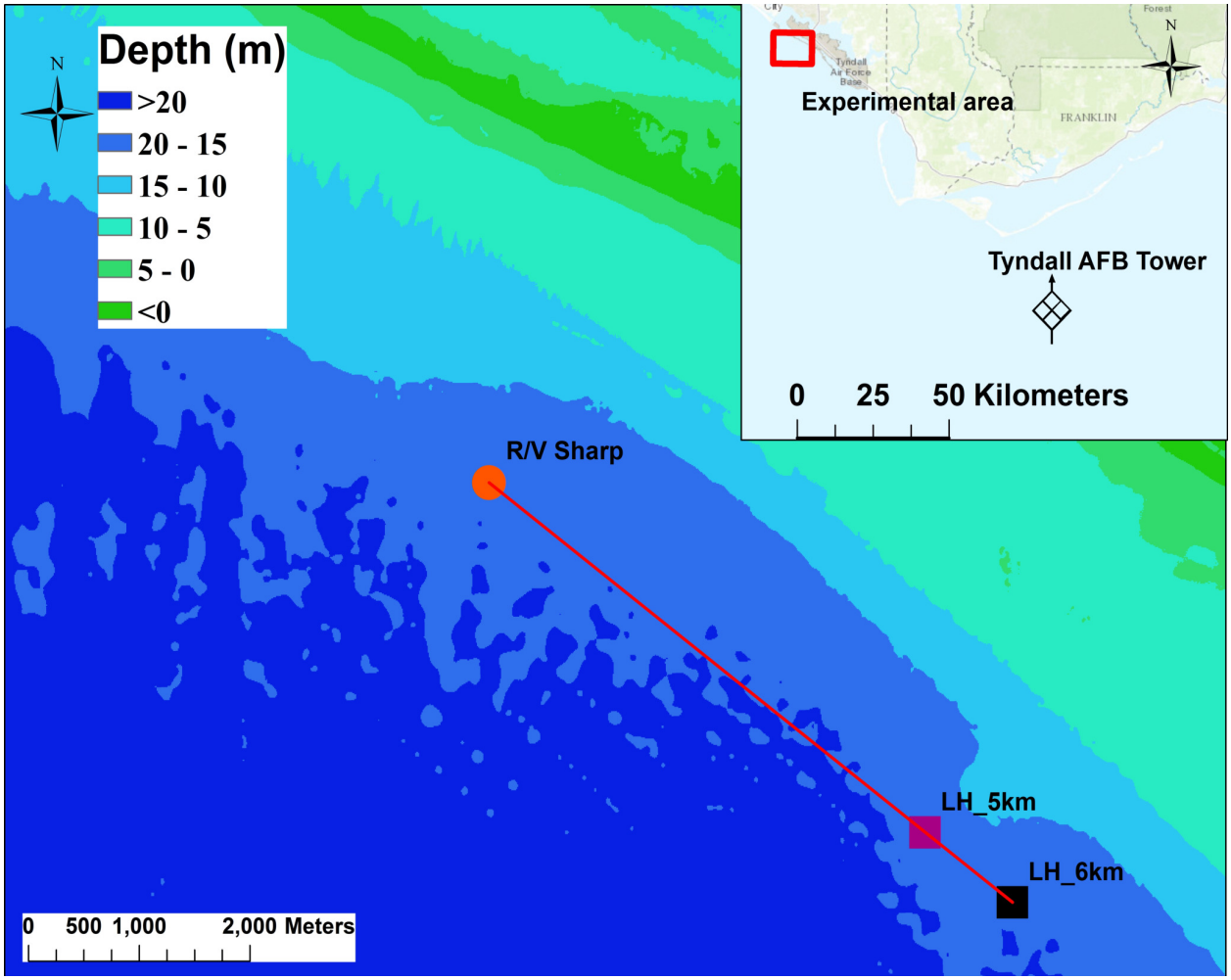

Figure 3.1: Bathymetry for the area and the relative locations of the underwater recording instruments. The research vessel where monostatic reverberation was being measured, the *R/V Sharp*, is shown as a red circle and the 5 and 6 km recording units are shown as purple and black squares, respectively. The location of the Tyndall AFB station [29° 24.5' N, 84° 51.5' W] that provided wind data is shown in the inset map. Bathymetry shown is a merged dataset comprising combining publicly available bathymetry [1] with data from an on-site survey conducted at the time of the TREX13 experiment [5].

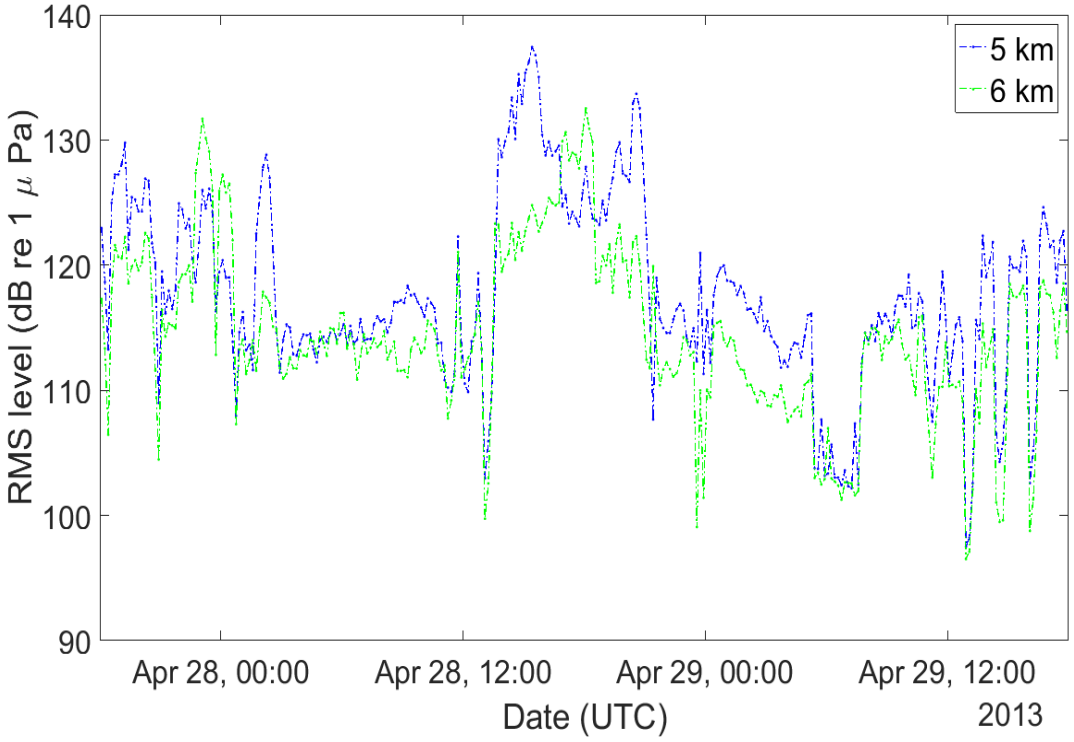

Figure 3.2: Comparison of 10-minute root mean square (RMS) levels in the 80 to 8000 Hz frequency band from April 27th 18:00 Z to April 29th 18:00 Z at the 5 km (blue line) and 6 km locations (green line). The occasional 10+ dB variation between the units is as a result of nearby experiment-related boat noise and active experimental transmissions.

related noise. Since the dominant background noise spectral levels were consistent, the 6 km data were selected for the discussion here due to the longer deployment period of this unit.

In Section 3.3.2 frequency domain trends are discussed. The longer deployment duration of the 6 km unit also meant that it collected data from May 1 to 6, 2013 when high winds were observed due to a storm in the area. This storm event is further discussed in Section 3.3.3.

Table 3.1: Acoustic Recorder Details

Unit	Hydr.Sensitivity	Gain	Sample Rate	Average Water Depth	Record Period
	(dB re 1V/μPa)	(dB)	(Hz)	(m)	(UTC)
5 km	-170.5	20	50,000	20	April 26 to 30, 2013
6 km	-169.7	0	20,000	20	April 24 to May 12, 2013

3.3 Background Noise Time Series-Results and Discussion

3.3.1 Trends in the Time Domain

Our characterization of background noise is presented in terms of the power spectral density (PSD) expressed in units of dB re 1 μ Pa^2/Hz where raw PSD estimates were generated from sequential non-overlapping 1 second data segments and averaged in 100 Hz frequency bands from 50 Hz to 8050 Hz. This was used to investigate the trend of 10-minute averaged root mean square (RMS) levels in the 80 to 8000 Hz band over the deployment period of the 6 km unit (Fig. 3.3 a). The storm phase of the deployment, May 1 to 6, 2013 was relatively free of experimentally-related noise since most related boat traffic left the area in anticipation of the high wind event. While some anthropogenic noise related to a fish survey is still observed, the variation in RMS level with time is reduced because of reduced boat activity.

This view of the broadband level can be compared with a time series view of the mean (linear average) and median power spectral density over a 100 Hz band centered at 3.5 kHz (Fig. 3.3 b and c). The time series of the linear average of 10 minutes of data in this band also shows elevated levels in the presence of experimentally-related noise. By contrast, the time series of the median of 10 minutes in the 3.5 kHz band agrees well with the linear average within the shaded region, but is much lower during times of increased experimental activity. This can be explained by the fact that the median is more resistant to high amplitude outliers than the mean. Additionally the relative consistency of levels throughout the median time

series suggests similar dominant processes influencing background noise levels. This will be investigated by considering trends in the frequency domain (Section 3.3.2).

3.3.2 Trends in the frequency domain

In this section we establish thresholds for the assessment of background noise levels in addition to further examining the trends observed in Fig. 3.3 in the frequency domain. The spectral probability density (SPD) gives the probability of observing a PSD level for a given center frequency within the range of observed values [26]. The SPD in this study is computed as follows: a sequence of 1 second PSDs are first estimated for the entire noise series for levels averaged in 100 Hz frequency bands from 50 Hz to 8050 Hz, then histograms of values of the PSD for each frequency bin (expressed in dB re 1 μ Pa^2/Hz) are constructed and subsequently combined and visualized across all frequencies as a shaded matrix of values. A higher SPD (darker colors on the SPD plot) here indicates a higher probability of observing a given spectral level for a particular 100 Hz frequency band. The addition of exceedance percentile lines for each bin indicates how often a level is observed in the dataset within that frequency bin. In a generalized sense, an exceedance percentile, L_x, indicates that the quoted level is exceeded x% of the time; therefore the L_{10} exceedance level is higher than the L_{90} exceedance level. The L_{50} exceedance level is the median and can be viewed as an indicator of typically observed levels. As applied to the SPD plot, if high values of the SPD (dark regions) fall along this line, this suggests that the median level is a good indicator of the most likely observed level within that frequency bin.

The benefits of this approach to this data analysis are at least two-fold, affording: 1) the ability to identify the underlying background noise levels in each band, despite the presence of transients such as experimental chirps and experimentally-related boat noise, and 2) the ability to identify interesting features in the spectra linked to dominant noise sources suspected to be biological in origin. It provides a summary view of the levels observed in the dataset from the lowest observed levels (the lower bound of the shaded area of the SPD plot) to the highest observed levels (the high bound of the plot). The averaging of PSDs

in 100 Hz frequency bands has the expected effect of smoothing the influence of signals of bandwidth less than 100 Hz but general trends will be unchanged. The darkest band in Figure 3.4 appears to be comprised of two regimes; the first can be traced by the narrowband L_{50} computed for periods during the day and the other is traced by the narrowband L_{50} exceedance levels for periods at night. The peaks below 1000 Hz seen in the narrowband L_{50} line are smoothed but the larger bandwidth peak between 4 and 5 kHz is preserved. The darkest band below 200 Hz would be better estimated by a low exceedance line such as the L_{90}. These levels may be used to obtain a range of spectral values to determine expected levels in the presence or absence of a noise source depending on the time of day.

For example, if we consider the selected time periods on April 25th (Fig. 3.5 a, purple (left) and blue (right) shaded areas), and the accompanying estimated PSD levels at a time within the selected periods (Fig. 3.5 b), these may be compared with the corresponding L_{50} exceedance levels for the narrowband case or the average of PSDs in 100 Hz frequency bins depending upon the bandwidth of the spectral signature being studied. This example case uses 100 Hz frequency bins. Comparison of the spectra shown in (left panel of Fig. 3.5 b) with the L_{50} shows that this is a time period when the noise source (in this instance, biological noise) is higher than the most likely observed level. In the absence of this noise mechanism (such as times in between biologically-related noise) the background noise level may be more suitably guided by the day L_{50} or L_{90} levels. The right panel (Fig. 3.5 b) shows that the example time period is a quiet period in the dataset since the levels at this time are below the median observed levels.

In concluding this section it is noted that levels in the 1.8 to 3.6 kHz frequency band and a 100 Hz frequency band centered at 3.5 kHz are consistent. For both bands, the L_{50} was 60 dB re 1 μ Pa^2/Hz and L_{90} was 54 dB re 1 μ Pa^2/Hz respectively averaged over day and night. Table 3.2 includes the day and night exceedance levels in these bands as well as a 100 Hz band centered at 4.5 kHz estimated from more than 600,000 PSD estimates based on 10 minutes of data. These values reflect our best estimate of background levels that are not influenced by noise from transmitted signals, expressed as exceedance levels.

Table 3.2: Summary of Exceedance levels (dB re 1 μ Pa^2/Hz) at the 6 km location for day and night for various bands of interest estimated from more than 600,000 independent samples of median values in 10 minute time segments.

L_x	f_c = 2.7 kHz		f_c= 3.5 kHz		f_c= 4.5 kHz	
	bw 1800 Hz		bw 100 Hz		bw 100 Hz	
	Day	Night	Day	Night	Day	Night
L_{10}	74	70	68	69	66	76
L_{50}	61	60	60	60	58	72
L_{90}	54	53	54	54	53	55

3.3.3 Storm Event

During the deployment period of the 6 km unit, the average wind speed was 5.3 m/s ±2.9 m/s. It is known that noise level dependence on wind speed is observable above a threshold [44], and that wind speed dependence can be masked by boat noise and biological activity [25] [28]. It is therefore desirable to focus attention on the May 1 to 6, 2013 time period when experimentally-related vessel traffic is reduced and the higher wind speeds allow some evaluation of wind dependence. However, continuous wind speed data in the experimental area is not available from May 1 to 6, 2013 because the storm event required temporary cessation of experimental activity, including the primary acoustic measurements, and the *R/V Sharp* therefore left the experimental area. Another research vessel, the *R/V Walton Smith* was periodically present in the experiment zone after the initial part of the storm period to conduct a fish survey. Wind speed data from the *R/V Walton Smith* from May 6-8, 2013, were compared with wind speed data obtained from the nearest open water National Data Buoy Center station, the Tyndall AFB Tower. This wind station is located approximately

100 km east of the experimental area [29° 24.5' N, 84° 51.5' W]. Since the anemometer height at this location is 35.1 m above mean sea level, wind speeds were converted to a reference height of 10 m above mean sea level using the Power Law Method [20] as a simplified means of exploring wind speed variation. The time series of wind speeds from this location compared well with wind speed measurements from the *R/V Walton Smith* with an orthogonal correlation coefficient $R = 0.68$, and this dataset is therefore deemed an acceptable surrogate to explore trends in wind-dependent noise during the storm period. While we are mindful that wind speed is not a precise measure of the sea surface conditions and the subsequent bubble formation that is the source of wind-generated noise, we investigate it here nonetheless in the absence of more suitable measures.

An examination of the data cloud of RMS levels in the 80 to 8000 Hz frequency band as a function of wind speed (Fig.3.6 a) shows that the lower bound appears to increase approximately 7 dB per doubling of wind speed. This is comparable to the roughly 6 to 7 dB increase per doubling of wind speed noted in other works [44], [32] and synthesized in [39] for a coastal location. The line shown in Fig. 3.6 (a) represents the 6 dB trend. We note that an estimate of the average RMS level in the 80 to 8000 Hz frequency band for a wind speed of 10 m/s taken from [39] is between 95 and 105 dB.

Finally it is of interest to note the effect of clustering these data with the goal of identifying dominant noise sources at a given time. For example, choosing the discretizing time-scale as 10 minutes, several features or attributes can be associated with a given 10-minute segment over the entire storm period, and time segments can be grouped together based on the similarity of their features. The clustering method selected was k-medoids [22] clustering. In the algorithm for this clustering method, the most representative or central segment for each cluster is selected from the existing data through a series of iterative optimization steps. An optimal set of clusters is created when the difference between members of each cluster is minimized. Since the choice of centroid is constrained to values within the dataset, this method is more resilient to outliers in the data, which could skew centroid placement.

The selected feature set consisted of 1) the wind speed, 2) the L_{10} levels, 3) the L_{50} levels

and 4) the L_{90} levels for each 10 minute segment within the storm. The clusters obtained from this method are shown in Fig. 3.6 as colored data points. Cluster 1 (red data) appears to follow a 7 dB increase per doubling of wind speed trend above a threshold wind speed while cluster 3 (blue data) does not appear to follow the squared relationship. A time series view of the three clusters (b in Fig. 3.6) shows that cluster 1 is primarily observed during quiet periods and this suggests that wind noise dominates the lowest levels. Cluster 2 is likely indicative of a mixture of processes influencing levels while cluster 3 is restricted to high amplitude events and is most prominently observed after sunset. Inspection of long-term spectrograms and listening to recordings from these periods suggests that biological noise is a prevalent noise source at this time.

3.3.4 Biophony

Biological noise within the dataset consisted primarily of sounds possibly related to fish or invertebrates, as well as vocalizations produced by unidentified dolphin species. The discussion here is limited to the major contributors up to 8000 Hz that result in diurnal peaks in the RMS level averaged in the 80 to 8000 Hz frequency band. These peak levels occur at astronomical twilight as shown in the 24-hour analysis of this frequency band covering April 24 to May 12, 2013 in a 24-hour clock view (Fig. 3.7 a, left) as well as a linear view including the span of L_{10} and L_{90} exceedance levels (Fig. 3.7 b, right). For this treatment of the data, histograms of 1-second RMS levels in the 80 to 8000 Hz band within 1 minute periods have been combined and visualized as a color-coded polar plot. The main body shows the relative number of times a given 1-second RMS level was observed at the specified time, with the sum of all bins equal to unity. Regions within the plot that tend towards the upper value of the colorbars may be interpreted as more stable estimates of the typical 1-second RMS level over the entire time period represented by the plot. As expected, most of the variability occurs between 13:00 Z and 22:00 Z -the peak experimental times. Shown in Fig. 3.7 a (left) are two pairs of thin, white lines each separated by 10 min (or 2.5°) in the 24 hr clock of the figure. These illustrate the variability of the onset and end of astronomical

twilight and show the alignment of diurnal peaks at these times, while the coloring of the outer circle indicates the phase of day progressing from full daylight (yellow) to night (black) with nautical and astronomical twilight periods shown as light and dark purple shaded areas respectively. Nautical twilight is the time in the day when the geometric center of the sun is between 6 and 12 degrees below the horizon and astronomical twilight occurs when the sun is between 12 and 18 degrees below the horizon. Over the time period analyzed, this biological noise was consistently present after sunset at 00:21 Z $\pm$ 10 min, subsequently peaking at the end of astronomical twilight 1:49 Z $\pm$ 10 min and persisting throughout the night hours. This was followed by a smaller peak again at the onset of astronomical twilight at 9:29 Z $\pm$ 10 min, prior to sunrise 10:57 Z $\pm$ 10 min. At the time of this writing the precise originators of these sounds cannot be conclusively stated, but they are interesting features for discussion because of the character of these sounds, their regular diurnal onset and their significant contribution to the mean square pressure at this time.

The spectral features, indicated by items 1 and 2 in Fig. 3.8, are responsible for the marked change in character of the average background noise spectra from day to night. The frequency bands containing these features, 100 to 1000 Hz and 4000 to 5000 Hz are responsible for the majority of the contribution to the mean square pressure averaged in the 80 to 8000 Hz band. This is illustrated in Fig. 3.9 which shows the contribution to total variance as a fraction of frequency for a time period at night when the RMS level was approximately 107 dB re 1 μPa. Approximately 75 % of the variance of the mean square pressure in the 80 to 8000 Hz frequency band is explained by the 100 to 1000 Hz and 4000 to 5000 Hz frequency bands. The spectral probability density plot previously discussed (Fig. 3.4) also highlights the influence of these sources within the background noise environment during the experimental period.

The first postulated biological sound is centered at 4.5 kHz, and is the likely source of the peak at 4.5 kHz noted as item 2 in Fig. 3.8 a showing the median spectral level at night. There have been reports of a similar persistent biological sounds at 6 kHz in Florida waters possibly related to the release of gas from swim bladders of members of

the *Clupeidae* family (such as sardines and herring) [36], [43]. There is some support for this as an explanation for the persistent 4.5 kHz sound in this dataset since several fish species with swim bladders were observed via a fixed camera system deployed during the experiment. These included: Tomtate (a type of "grunt" fish, *Haemulon aurolineatum*), Round scad ("cigar minnow", *Decapterus punctatus*), and Atlantic spadefish ("angelfish", *Chaetodipterus faber*) [36], [37]. Fish may not be the only possible biological originators of the two observed acoustic signatures. Some invertebrates have also been observed to create similar diurnal variations. In particular, a species of the *Maja* genus (hermit crab) has been reported to elicit a sound associated with feeding with a PSD level of approximately 80 dB re 1 μ Pa^2/Hz) for a frequency band comparable to the 4.5 kHz sound discussed here [8].

The second postulated biological sound, in the 100 to 1000 Hz frequency band, exhibits prominent frequency peaks at approximately 210, 350 and between 600 and 700 Hz. This call (for which a pressure time series is shown in Fig. 3.8 c) does not appear to be consistent with known sounds associated with the fish species observed via the deployed camera system, but does resemble a documented call from a sea robin species [7], [42]. While there is no visual confirmation of the presence of this species, (of the *Triglidae* family), the observed call does fall within the range of frequencies for a documented *Triglidae* call with a fundamental frequency range of 174 to 217 Hz with harmonic peaks of 348 to 481 Hz and 522 to 674 Hz as noted in [7].

3.4 Summary

In this paper the background noise levels during TREX13 were presented in terms of exceedance levels where L_x indicates that the quoted PSD level is exceeded x% of the time. Daily and overall trends within three frequency bands were explored. The L_{50} was 60 dB re 1 μ Pa^2/Hz for both the 1800 to 3600 Hz frequency band as well as a frequency band centered at 3.5 kHz of 100 Hz bandwidth averaged over day and night. Contributions to the background level from suspected biological sources were investigated and the frequency range of one of the diurnal biological signals makes it significant to the analysis of TREX13

experimental signals since it is within the 1 to 10 kHz band and is consistently present after dusk and before dawn. An approximate 10 dB difference in peak levels was observed between the end and onset of astronomical twilight with the lowest levels observed immediately after dawn. The data suggest that the lowest noise levels are constrained by wind above a threshold in the absence of biological and anthropogenic masking noise.

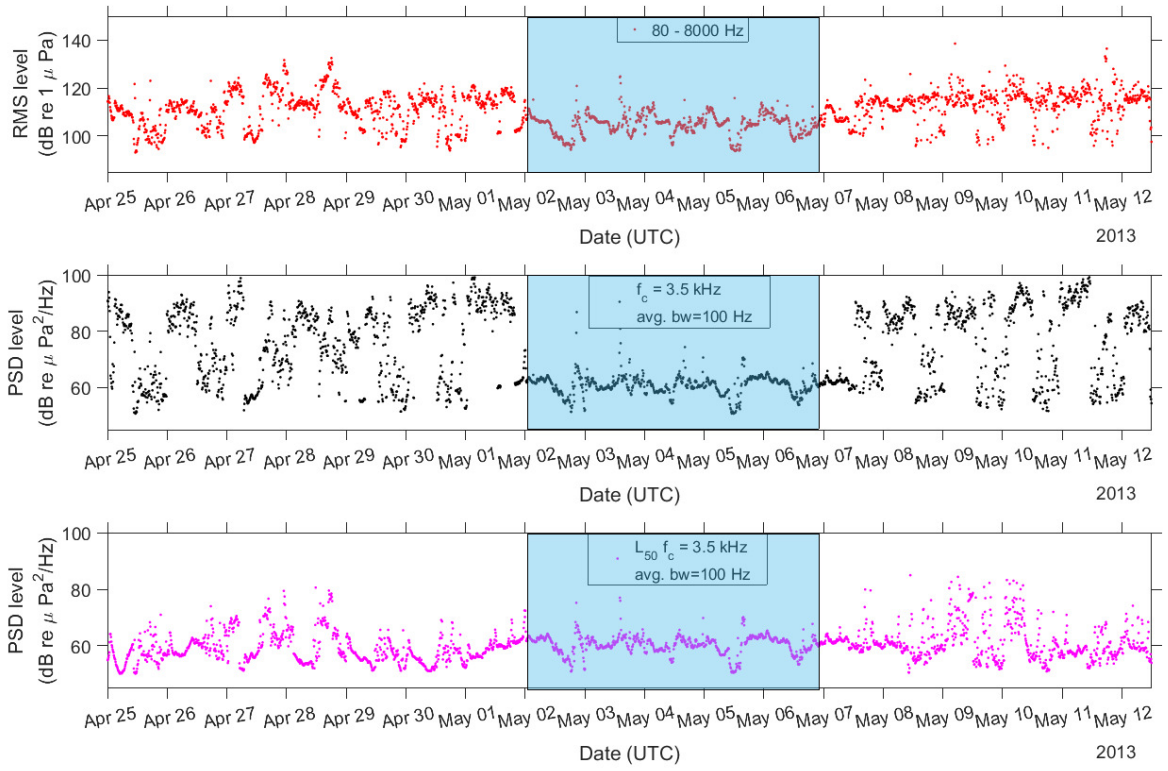

Figure 3.3: Comparison of time series of a) RMS levels in the 80 to 8000 Hz band at the 6 km site from April 25 to May 12, 2013 and b) the power spectral density in a 100 Hz band centered at 3.5 kHz. Note that fluctuations in this frequency band outside of the storm period are primarily due to active TREX13 transmissions. In panels a and b each point is the linear average of 600 1-second estimates. The time series of power spectral density can be compared with c) the median PSD over a 100 Hz band centered at 3.5 kHz for time bins of 10 min; each point in panel c represents the median PSD of 600 1-second samples. The shaded region represents the time period when experimentally-related noise was greatly reduced and overlaps with the storm period May 1 to 6, 2013. The time series of the median level in the 3.5 kHz band agrees well with the linear average within the shaded region but is much lower during times of increased experimental activity. This may be better understood by considering trends in the frequency domain.

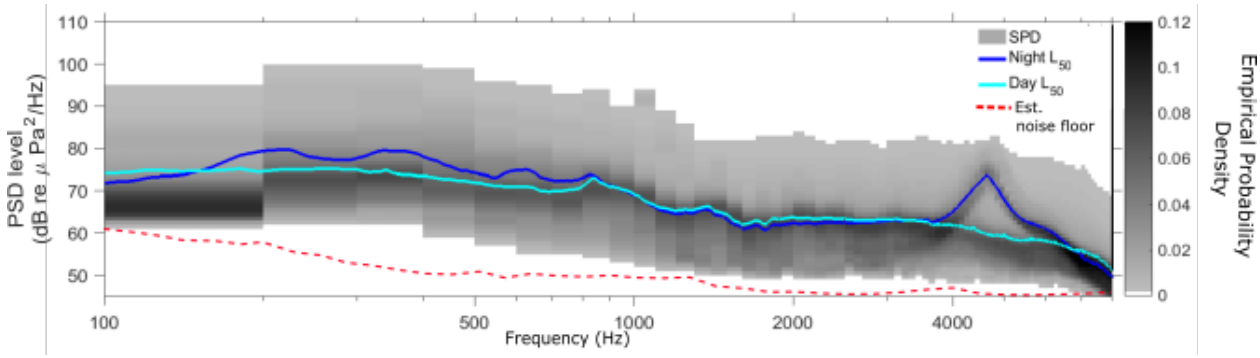

Figure 3.4: SPD plot of 6 km data for the period April 24th 00:00 Z to May 12th 00:00 Z. The darkest regions indicate the most often observed spectral levels averaged over frequency bins of 100 Hz for a given frequency bin in this shaded histogram view of the data. The overlaid lines show the L_{50} lines for day (light blue line) and night (dark blue line. The estimated instrument noise floor levels are indicated by the red dashed line. The L_{50} lines for night and day trace most of the darkest regions of the plot and indicate that the median is a good descriptor for likely observed levels.

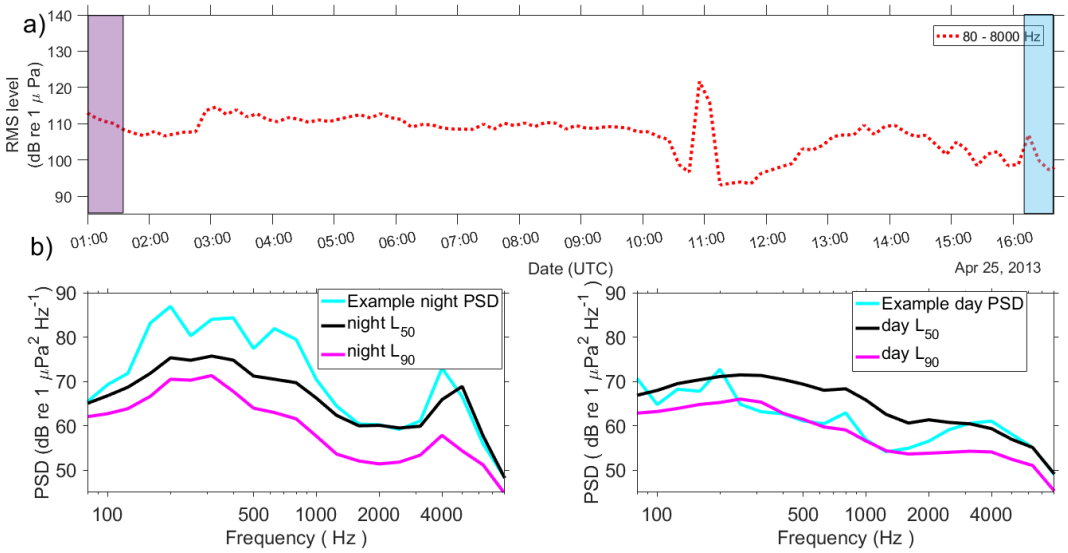

Figure 3.5: Illustration of decision process for designating background noise levels guided by the SPD plot. Considering a) example time periods at night (left purple shaded area) and day (right blue shaded area) on April 25th, b) measured PSD levels for the night (left) and day (right) can be compared with the corresponding L_{50} and L_{90} for the time of day.

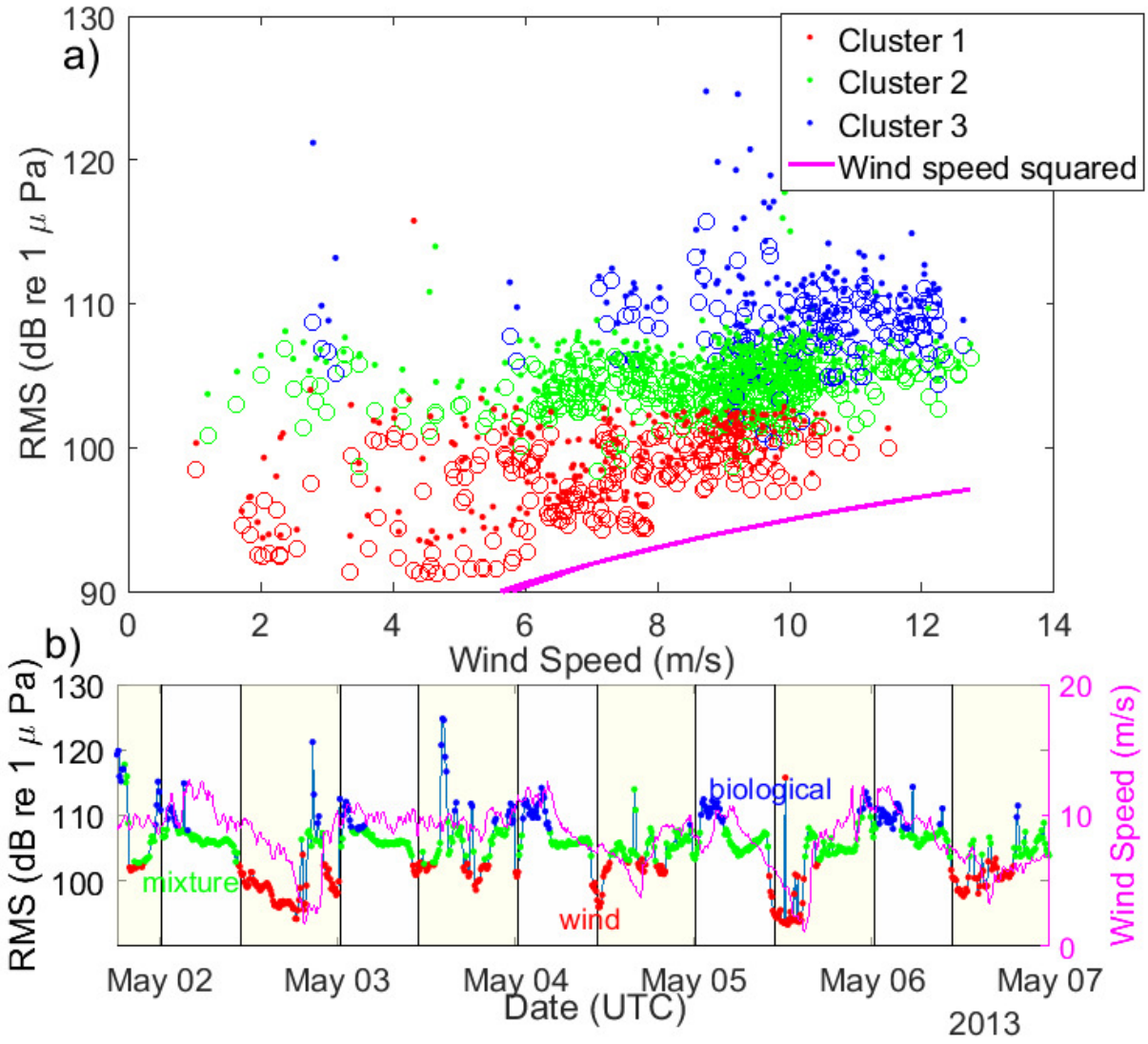

Figure 3.6: a) RMS levels in the 80 to 8000 Hz frequency band as a function of wind speed. The magenta line shows the trend of squared wind speed. The data points are colored to represent different clusters derived from a k-medoids clustering of data during the time period May 1 to 6, 2013. The open circles indicate the L_{90} RMS level within a given cluster and the solid points indicate the 10-minute average RMS level. Cluster 1 (red dots) exhibits wind dependence above a threshold while cluster 3 (blue dots) does not readily show this trend. Each point can be associated with a particular time so a b) time series view of the clustered data can be obtained. Cluster 1 is primarily associated with the lowest levels suggesting that wind (magenta line) is the dominating noise mechanism at the quietest times. Cluster 3 is prominently observed after dusk (unshaded regions) and is likely related to biological noise at that time.

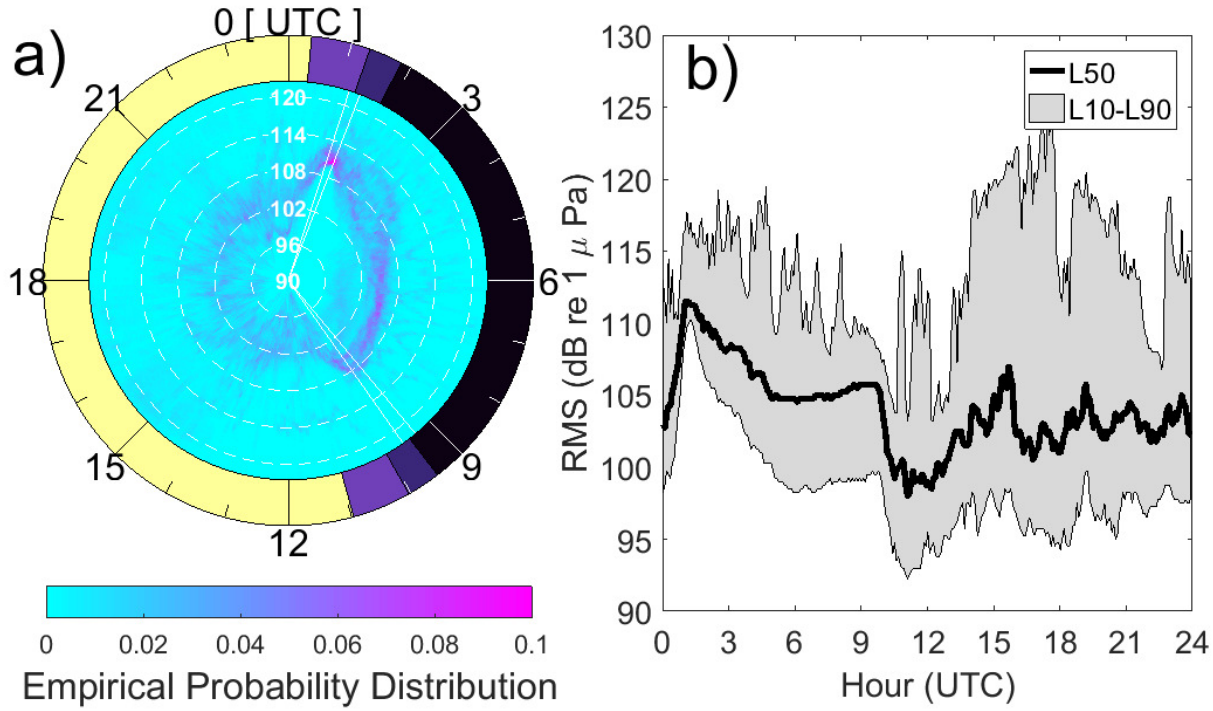

Figure 3.7: a) 24-hour analysis of 80 to 8000 Hz frequency band covering April 24 to May 12, 2013 as a polar plot. The white banding lines illustrate the variability of the onset and end of astronomical twilight and show the alignment of diurnal peaks at these times. The coloring of the outer band indicates the phase of day progressing from full daylight (yellow) to nautical twilight (light purple) to astronomical twilight (dark purple) to night (black). b) showing the 24-hr L_{50} trend as a black line bounded by a grey shaded area indicating the span of the 10th and 90th exceedance levels for 1 minute time periods. Both views show an approximate 10 dB difference in peak levels between the end and onset of astronomical twilight and levels are lowest immediately after dawn.

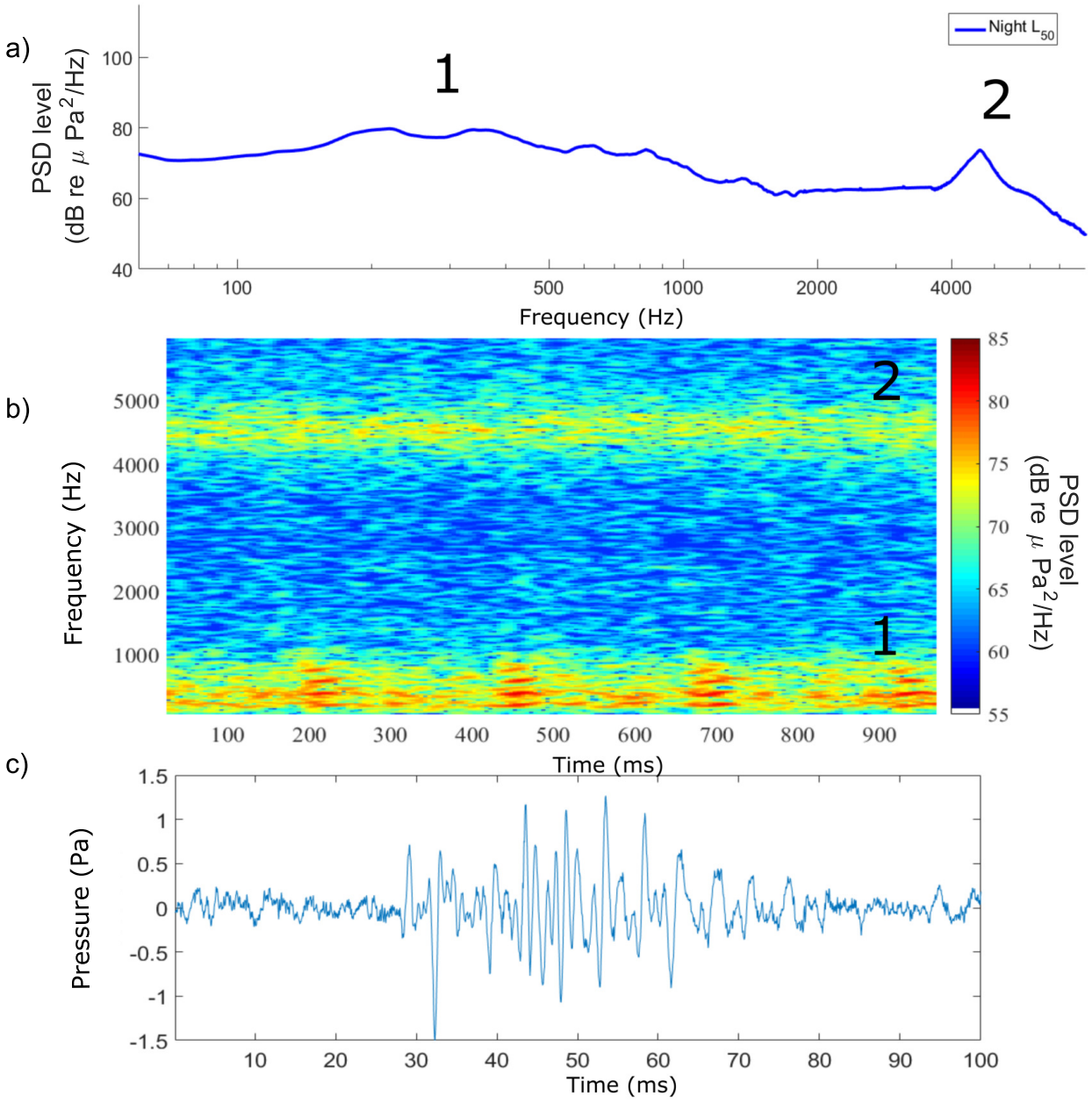

Figure 3.8: a) The night L_{50} power spectral density for the 6 km dataset showing peaks at frequencies that correspond to peak frequencies in the dominant biological calls (item 1) and the center frequency of the biological sound centered at 4.5 kHz (item 2). b) A spectrogram generated from 1024 point Hanning-windowed Discrete Fourier transform (DFT) with 90% overlap shows the dominant biological sounds identified within the dataset (items 1 and 2 from a) and c) is an example time series of one instance of a biological call (as illustrated by item 1 in a) at night.

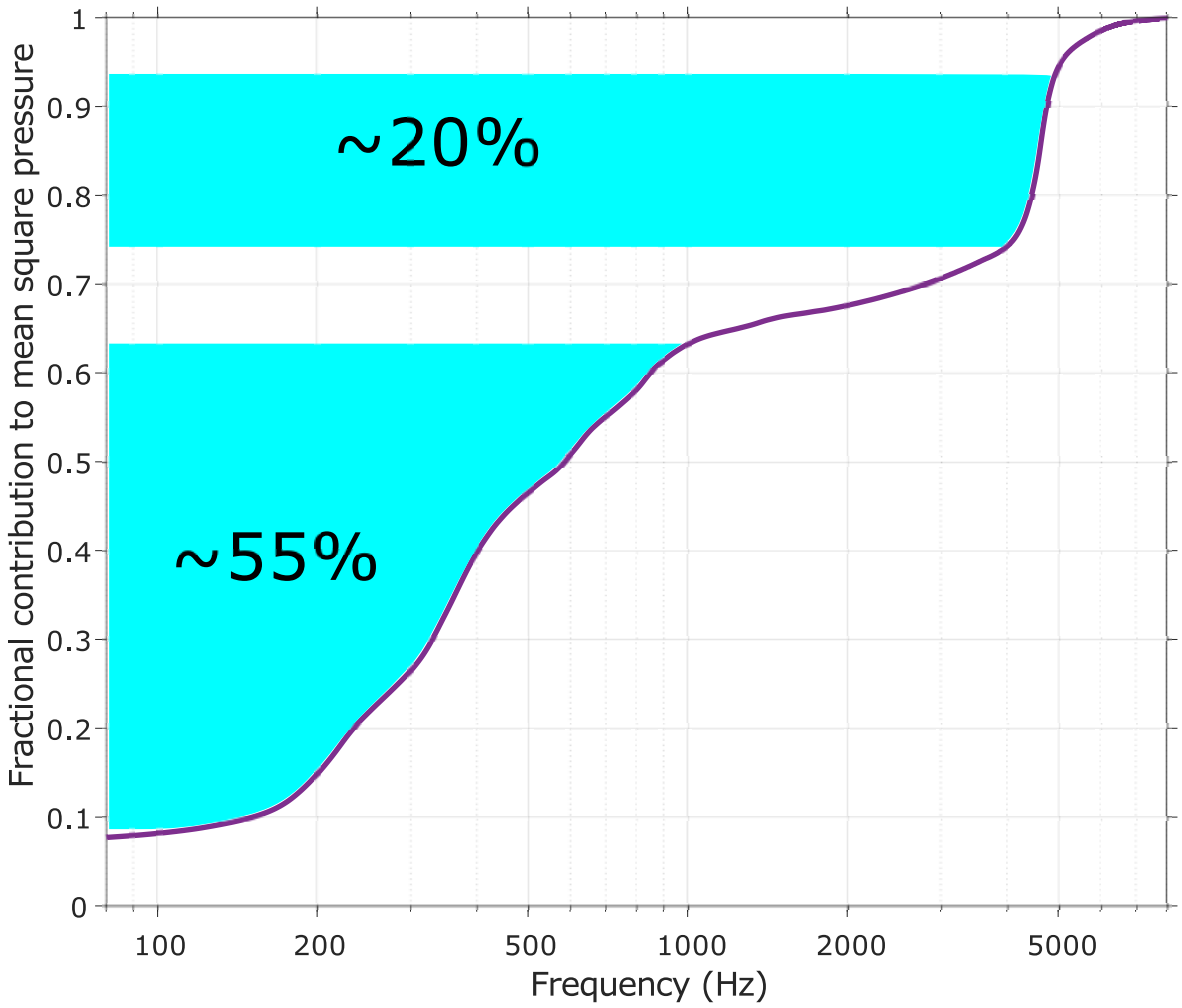

Figure 3.9: Showing the contribution of total variance as a function of frequency for a typical spectrum at night when biological sounds were present. The 100 to 1000 Hz and 4000 to 5000 Hz frequency bands contribute to approximately 75 % of the variance of the mean square pressure in the 80 to 8000 Hz frequency band.

Chapter 4

MODELING: BACKGROUND NOISE TRENDS AND THE DETECTION OF CALVING EVENTS IN A GLACIAL FJORD

4.1 Introduction

Calving has been identified as one of the most important processes controlling ice loss [2], and improvement of estimates of calving rates will lead to improvements in models for estimating sea levels.

Each phase of a calving event is spectrally distinct, and the particular frequencies and durations of each phase depend on the size and location of the calving event as well as the glacier and fjord characteristics [31]. For calving events, the main source of underwater noise from the splash of the ice entering the water are the impact and passage of the ice through the water surface, the resonance vibrations of the body and the volumetric pulsations of the closed cavities of air entrained during the entry [15].However, sound is also radiated underwater when bubbles, originally trapped during glacier formation, are released as a jet or as squirting events from ice orifices [23]. Characteristic frequencies have been identified for the spectral range associated with bubble release through laboratory experiments [23], and have been confirmed to be between 1 kHz and 3 kHz [17]. The difficulties associated with identifying calving events have been previously discussed [16]; noise levels can be expected to be heavily dependent on the temporal and spatial distribution of ice in the fjord as well as dominant propagation characteristics. However, to date, no estimations of source spectral levels have been presented, which could be useful as part of a growing body of observations of calving events leading to source models of calving events.

In this work, underwater noise in a glacial fjord was measured and the data were analyzed to determine time periods associated with calving noise. The utility of spectral probability

density in evaluating background noise characteristics in the frequency domain is illustrated and nominal source spectral levels of calving events observed within a glacial fjord in western Greenland are calculated. The utility of an unsupervised classification method (k-medoids clustering) is also demonstrated for data exploration. We suggest that clustering may be helpful for informing the pre-processing of acoustic data, prior to the implementation of more complex algorithms.

Section 4.2 discusses the analysis methodology. It includes details of experimental setup and recording system characteristics (Section 4.2.1), details of the parameters used within the parabolic equation model (Section 4.2.2), the approach to statistical modeling of ambient noise (Section 4.2.3) and the application of k-medoids clustering (Section 4.2.4). The results from the analysis are presented in Section 4.3 and a summary and additional comments are presented in Section 4.4.

4.2 Methods

4.2.1 Description of Field Observations and Equipment Settings

The acoustic measurements discussed in this work were collected in the Sarqardleq Fjord in Greenland (Figure 4.1) from 24-29 July, 2013. Acoustic data were collected in time series form using an autonomous acoustic recorder (Loggerhead Instruments, Inc.). The unit was equipped with a hydrophone of nominal receive sensitivity -171 dB 1 V/μPa and was set to continuously record at a sampling rate of 50 kHz with zero gain. The frequency response of the recording unit is approximately flat over the frequency band 80 Hz to 8000 Hz and data were corrected using the manufacturer-provided gain curve. The acoustic data have been archived and made publicly available [10]. These measurements were collected along with in-situ surface wave and oceanographic measurements, complemented by aerial and satellite photographs by a team from the Woods Hole Oceanographic Institute (WHOI) [41].

The deployment and recovery locations are shown in Figure 4.1a. The recorder was moored 11 m below the surface. The bathymetry at both location was similar and average

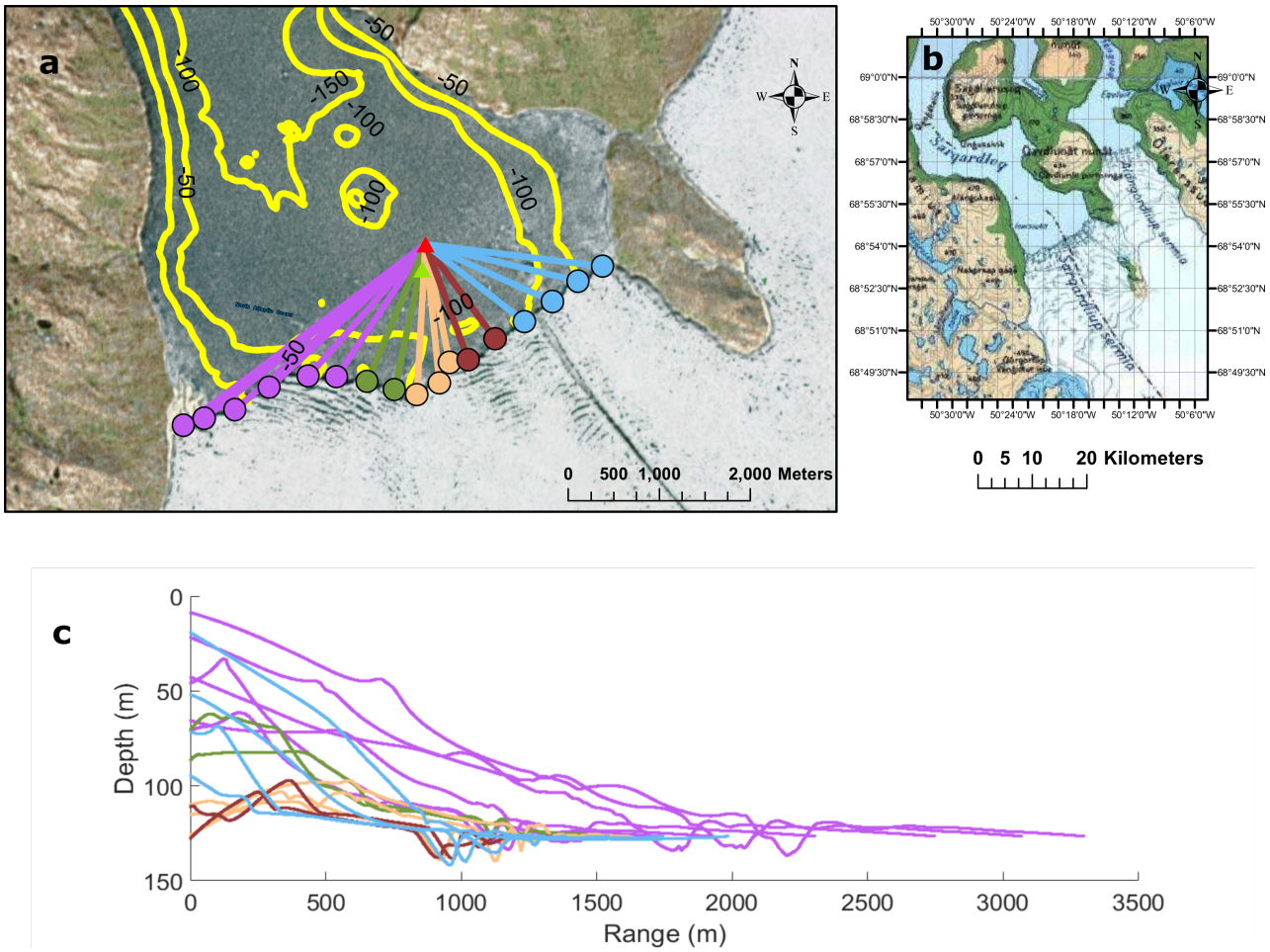

Figure 4.1: a. The location of the instrument in relation to the glacier face is shown. The mooring (original deployment location shown by the green triangle) moved during the deployment period and was recovered approximately 250 m (red triangle) from the original deployment location. The depth at the mooring location was approximately 125 m. Also shown here are 17 transects (roughly grouped in increments of 30 degrees) emanating from the base of the glacier to the recorder's recovery location. b. An overview of the geographic location of the Sarqardleq Fjord. c. Depth and range for each group of transects; these depths and ranges were used in acoustic modeling. Map Service Layer Credits: ESRI, HERE, Garmin, OpenStreetMap contributors and the GIS user community. Map Source: ESRI, DigitalGlobe, GeoEye, Earthstar Geographics, CNE/Airbus DS, USDA, USGS, AeroGRID, IGN

conditions based on both locations were used for subsequent acoustic modeling.

4.2.2 Simulating the Propagation Environment and Estimating Calving Source Spectra

Six calving events, identified aurally (and confirmed photographically by the WHOI team), were studied in order to determine spectral levels that could be expected in the nominal vicinity of the source. It is necessary to consider the propagation conditions for this fjord at the range and depth of the recorder in order to infer the source spectral levels from the received spectra at the location of the recorder. Bathymetric data were collected via autonomous underwater vehicle by the WHOI team and were utilized for this analysis. Further details regarding bathymetric data collection and processing are available in [38]. Seventeen transects (Figure 4.1 c) were used to extract depth and range values to model the spatial variation of the acoustic intensity.

The nominal sound speed profile (Figure 4.2) was estimated using conductivity, temperature and depth (CTD) data [38] using the Del Grosso equation, noted to be applicable for arctic conditions [13]. The resultant sound speed profile indicates a region of ducted propagation. Somewhat similar sound speed profiles were noted for July in an eastern Greenland fjord [35]. In that survey the authors observed an average summer sound speed profile which was mixed with a minimum sound speed at mid-water depth. The sound speed profile observed in the Sarqardleq Fjord during the experiment was also mixed, but the minimum sound speed occurred at approximately 20 m.

The Green's function, $G(f, z_0, z_r, R)$, represents the transfer function connecting a source, z_0, and receiver (depth, z_r and range, R), for a particular frequency, f, and embodies the loss of acoustic intensity with range from source. Transmission loss increases with increasing range and is defined as -10 $\log_{10}|G(f, z_0, z_r, R)|^2$ in this study. The Range-dependent Acoustic Model parabolic equation (RAM-PE) code [6] was used to compute $G(f, z_0, z_r, R)$ over a grid defined every 1 m in range and 0.1 m in depth using the parameters listed in Table 1. The acoustic values in Table 1 were selected to emulate a sandy-silt layer overlying bedrock. A similar propagation environment was reported by [35] for an East Greenland

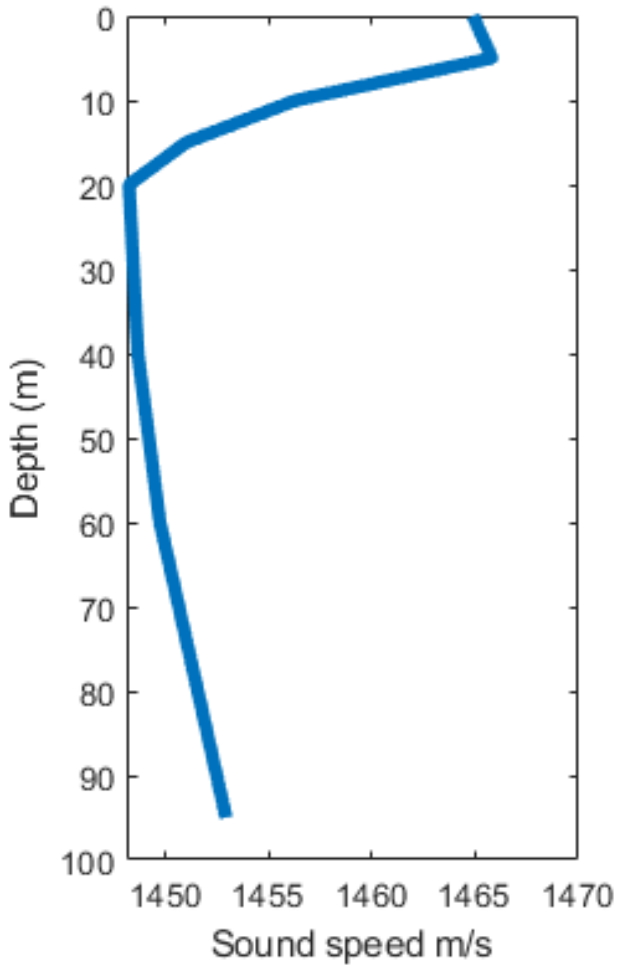

Figure 4.2: Estimated sound speed profile derived from CTD data [38]. The sound speed profile observed in the Saqqarliup Fjord during the experiment was mixed; the minimum sound speed occurred at approximately 20 m.

fjord. We utilize similar compressional wave speeds, attenuations and densities from their work - with the exception of the compressional wave attenuation in the sandy-silt layer, which was set at 0.6 dB/λ. This value is within the range used in an equivalent fluid approximation [45] for low shear speed seabeds (though we neglect the effect of a complex density in our implementation). Also, given the inability to set shear speeds in the model, the value was chosen to approximate the influence of shear in the sand layer. The depths of each layer are also included in the table; the zero depth here denotes the end of the water column and the beginning of the sediment environment.

Table 4.1: Geoacoustic parameters for modeling

Bottom type	Compressional speed	Compressional attenuation	Density	Layer Depth
	(m/s)	(dB/λ)	(g/cm^3)	(m)
Layer 1-sandy-silt	1575	0.6	1.6	0 - 155
Layer 2 - bedrock	2000	0.4	2	155 - 350
Absorbing layer 1	2000	10	2	350 - 400
Absorbing layer 2	2000	20	2	400 - 500

An estimation of the average transmission loss at the recorder location is required in order to derive nominal source spectra. Ice that breaks off from glaciers has a wide distribution of sizes and are classified based on both their height above sea level and the surface area covered. Heights above sea level range from less than 1m for smaller pieces of ice, while medium to large fragments ranging from 1m to 5m above sea level and the largest fragments (classed as icebergs) extend more than 5 m above sea level. It has been observed that most most ice masses are between 5 to 20 m in length with few calved blocks greater than 10 m [9]. Therefore, for the purposes of modeling we have used sources distributed at uniform intervals of one meter to 10 m in depth at the glacier face and $|G(f, z_0, z_r, R)|$ was computed for frequencies ranging from 20 Hz to 3000 Hz. Then, for each frequency, $< |G(f, z_0, z_r)|^2 >$ at the receiver location was computed using an averaging box with a width defined by the

last 100 m of range and centered at a z_r of 11 m, extending $\pm$ 5 m for each transect. This was then repeated for all source depths and the resulting estimates were averaged over all source depths. This final averaged quantity is therefore a function of frequency only and will be denoted by $< |G(f)|^2 >$, while -10 $\log_{10} < |G(f)|^2 >$ will be denoted by H_{av}.

To estimate the uncertainty in H_{av} for a given frequency, f, and consequently uncertainty in the estimation of calving source spectra, we follow a formal pathway suggested by [3]. First we determine a normalized standard deviation or coefficient of variation, V, which quantifies the size of fluctuations relative to $< |G(f)|^2 >$ and is given by:

$$V = \sigma(|G(f)|^2) / < |G(f)|^2 >, \tag{4.1}$$

where $\sigma(|G(f)|^2)$ denotes the standard deviation of $< |G(f)|^2 >$. Using V, we obtain the bounds H_+ and H_- for all 17 transects with respect to H_{av} via:

$$H_\pm = H_{av} - 10 \log_{10}(1 \mp V), \tag{4.2}$$

The median values of H_+ and H_- and H_{av} were used for the final operational values. These bounds were applied to correct the received spectra of calving events to infer possible source spectra for calving events. Examples of H_+, H_- and H_{av} for specified frequencies and the resultant corrected spectra are discussed in Section 3.

4.2.3 Analysis of Frequency and the Use of Probability Distribution Functions

The analysis in this paper is derived from a series of one-second power spectral density estimates (PSDs) of the mean square pressure. The data were demeaned and normalized such that the integral of the one-second spectrum was the mean square pressure of the data. After normalizing, the spectra were truncated to 10 kHz since the majority of the mean square pressure is captured in this band. Although the recorder was deployed from 24-29 July we focus on the 25-28 July time frame which is generally free from noise associated with deployment and recovery of the mooring.

These calibrated spectra are based on one second of data (no overlap and no windowing); this implies that any particular spectral estimator is a random variable (RV) with a chi-square distribution with two degrees of freedom (DOF) [30], or, equivalently, the exponential distribution. We deliberately choose to preserve this property by foregoing any further averaging (which would smooth the spectra), and these spectra are used in the computation of the empirical spectral probability density (SPD).

The spectral probability density (SPD) gives the probability of observing a PSD level for a given center frequency within the range of observed values of, $s = 10\ \log|X_f|^2$, [26]. The SPD in this study is computed as follows: a sequence of one-second PSDs is first estimated for the entire noise series (as previously discussed), then histograms of values of the PSD for each frequency bin (expressed in dB re 1 μ Pa^2/Hz) are constructed and subsequently combined and visualized across all frequencies as a shaded matrix of values.

A higher SPD indicates a higher probability of observing a given spectral level for a particular 1 Hz frequency band. The addition of exceedance percentile lines for each bin indicates how often a level is observed in the dataset within that frequency bin. In a generalized sense, an exceedance percentile, L_x, indicates that the quoted level is exceeded x% of the time; therefore the L_{10} exceedance level is higher than the L_{90} exceedance level. As applied to the SPD plot, if high values of the SPD fall along a particular exceedance level line, this would suggest that that given exceedance level is a good indicator of the most likely observed level within that frequency bin.

Since the spectral magnitudes, $|X_f|^2$, are exponentially distributed it is possible to adopt the use of a theoretical probability density function (PDF) that has been used to investigate decibel quantities such as s [12], where the authors utilized this PDF in the analysis of sonar and radar data.

The PDF for s accommodates the fact that λ, the mean value of $|X_f|^2$, may itself slowly vary in time and takes its own distribution of values given by the following:

$$p_\lambda(\lambda) = \frac{e^{-(log\lambda-\mu_1)^2/(2\sigma_1^2)}}{\sigma_1\lambda\sqrt{2\pi}} \tag{4.3}$$

The parameters in Equation 4.3, μ_1 and σ_1, are discussed subsequently.

The aforementioned PDF developed for s is given by:

$$p_s(s) = \int_0^\infty p_{s|\lambda}(s|\lambda)p_\lambda(\lambda)d\lambda \tag{4.4}$$

where the conditional PDF is:

$$p_{s|\lambda}(s|\lambda) = \frac{e^{-e^{\frac{s/k}{\lambda}+\frac{s}{k}}}}{k\lambda} \tag{4.5}$$

The mean, $E(s)$, and variance, $Var(s)$ of the PDF in Equation 4.4 are also computed by [12] and are:

$$E(s) = \mu_T - C_E k \tag{4.6}$$

$$Var(s) = \sigma_T^2 + \frac{k^2\pi^2}{6} = \sigma_T^2 + 5.57^2 \tag{4.7}$$

where C_E is Eulers constant (0.577215), k is 10 $\log_{10}e$, $\sigma_1 = \sigma_T/k$ and $\mu_1 = \mu_T/k$. Equations 4.6 and 4.7 are utilized to obtain μ_T and σ_T in fitting Equation 4.4 to empirical histograms.

The effect of the slow variation is the addition of σ_T^2 to an underlying variance of 5.57^2 dB^2. We postulate that s ($10\log_{10}|X_f|^2$) for frequencies, f, that are within the higher frequency band related to ice melt, 1000 to 3000 Hz, (previously discussed in Section 4.1 and a persistently steady feature of the background noise environment) will have a standard deviation that closely approximates 5.57 dB. We also postulate that lower frequency bands related to ice calving will have standard deviation much greater than 5.57 dB.

This new parameter, σ_T, was studied on time scales of 24 hours to identify frequency bands of interest, and 1 minute for use as a feature in the context of k-medoids clustering. For this, we will focus on the bands with the highest values of σ_T to be discussed further in Section 4.3.2.

4.2.4 Automated Identification of Time Periods for Labeling of Calving Events: an Application of k-medoids Clustering

Clustering is used for exploration, organization and may be used in cases where the number of classes/clusters is unknown. Often, subject matter knowledge may be used to further study the result from a clustering method. The choice of clustering method and strategy strongly depends on the end goal and the context of the analysis. Additionally, clustering is often a precursor to predictive models, acting as the "teacher". Our focus here is on statistical learning as a means of data exploration and as such we do not place emphasis on algorithm training; these methods are meant to inform the decision making process on the selection of features on which to base training by facilitating a systematic study of the noise dataset being analyzed. Comprehensive summaries and guidance on the use of clustering can be found in recent publications [19].

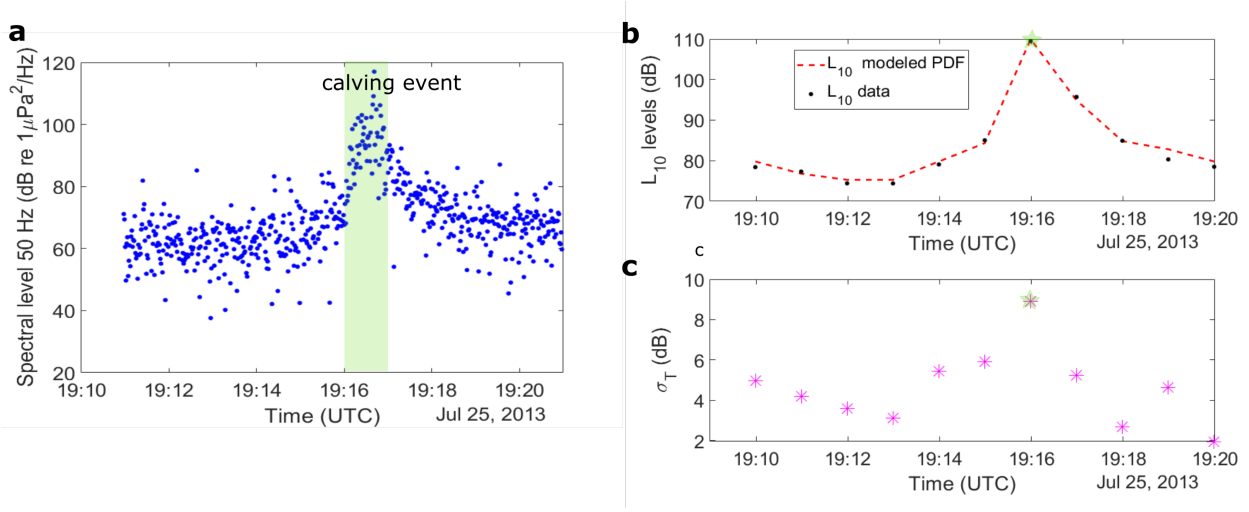

Figure 4.3: Illustrating calculation of features used for clustering. a. The spectral levels in the 50 Hz frequency band for a time period containing a calving event on 25 July, 2013. The corresponding L_{10} (b) and σ_T (c) for a particular one minute period (green shaded area) are indicated by green stars.

In the current case, k-medoids clustering [22] is used to explore the data to identify

interesting patterns and then determine which, if any, can be correlated with observed calving events that have been photographically confirmed (to the nearest minute). Several features or attributes can be associated with a given minute segment over the entire deployment period, and time segments can be grouped together based on the similarity of their features. For example, Figure 4.3 illustrates the calculation of features for a particular frequency band (50 Hz). A ten-minute period on 25 July, 2013, containing a calving event is shown. For a given minute (green shaded area), the L_{10} and σ_T features can be calculated and we propose using k-medoids to group data based on the similarity of their L_{10} and σ_T values for frequency bands of interest.

In the k-medoids algorithm the most representative or central segment for each cluster is selected from the existing data through a series of iterative optimization steps. An optimal set of clusters is created when the difference between members of each cluster is minimized. Since the choice of centroid is constrained to values within the dataset, this method is more resilient to outliers in the data which could skew centroid placement to a position outside of the primary cluster.

The objective of the k-medoids algorithm is to partition the data into k clusters or groups where k is the number of groups required by the user. The choice of the number of clusters is a decision made by the user and the final choice might be based on visual inspection of the data where obvious clusters exist, the user's knowledge of the dataset and expected patterns that could be found or a systematic trial and error study of the partitioning that occurs when various values of k are used. In the latter it is common to then, for example, employ a silhouette analysis [34] to visualize the compactness of clusters. At the center of each group is the medoid: a point from the dataset which minimizes the dissimilarity between that point and all other members of the cluster. The measure of similarity (or distance metric) varies from problem to problem. In the current case, two distance metrics were evaluated: the mahalanobis distance and the correlation distance.

If the center of a cluster is denoted by c and a given point in the dataset is denoted by h, then the mahalanobis distance, d_m, is given by:

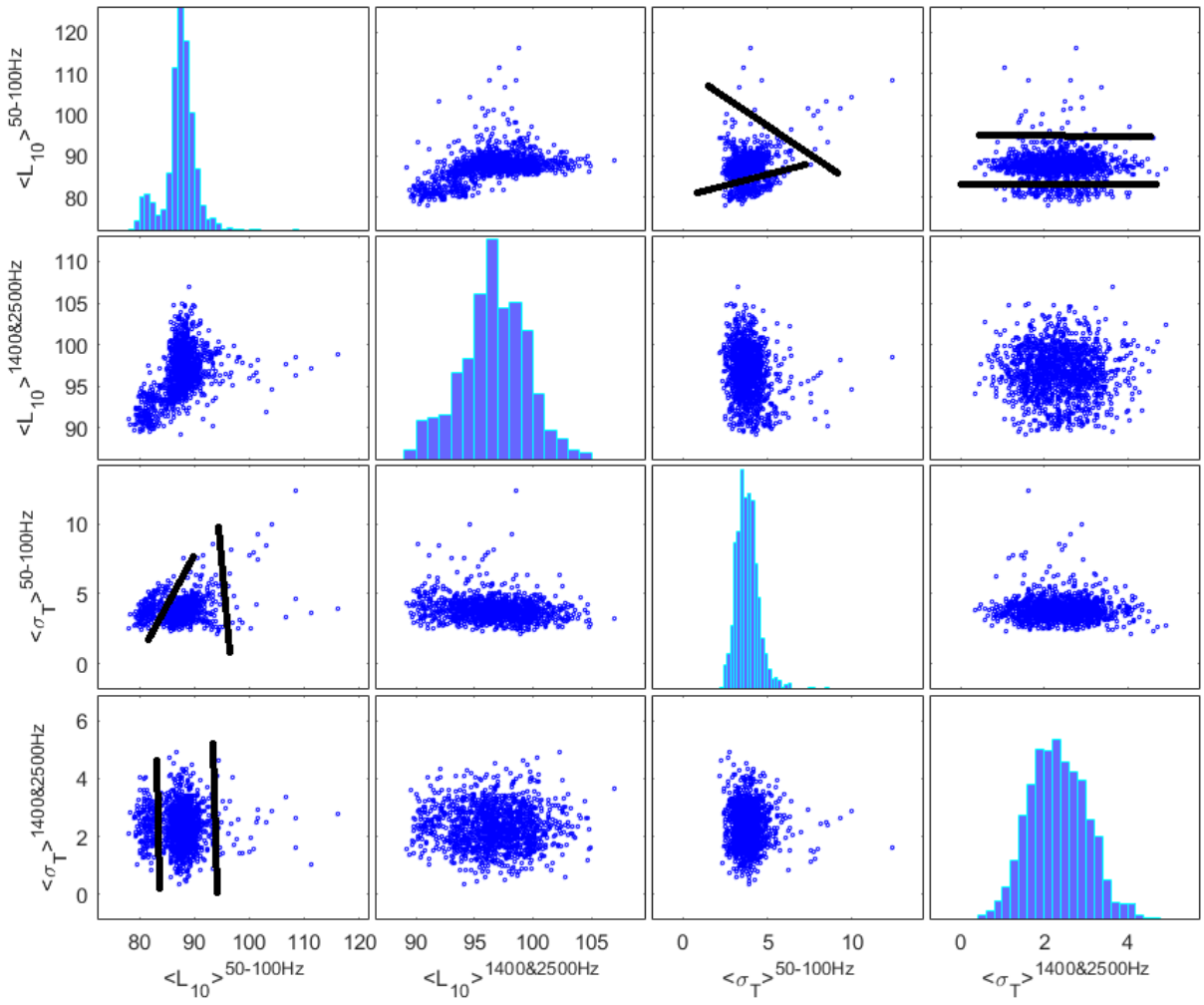

Figure 4.4: Scatter plot matrix showing relationships between paired combinations of the four features selected for study for 28 July 2013: the average L_{10} levels for frequencies from 50 Hz to 100 Hz, the average L_{10} levels for frequencies 1400 and 2500 Hz, the average σ_T for frequencies from 50 Hz to 100 Hz and the average σ_T for frequencies 1400 and 2500 Hz. In the figure, the <> notation indicates an ensemble average over either the calving frequency band (50 -100 Hz) or the two higher frequency bands (1400 and 2500 Hz). All features are calculated on a time scale of one minute; each scatter plot contains 1440 points; notional separations of clusters are indicated by the black lines. The diagonals of the plot are histograms of each feature.

$$d_m(h,c) = \sqrt{(h-c)^T S^{-1}(h-c)} \tag{4.8}$$

where S is the covariance matrix of h and c. This choice of distance metric allows for clusters where the variance is not of the same order of magnitude in all dimensions i.e. clusters that are not spherical. In our current case, we are interested in outliers in the dataset and will be helped by methods that correctly represent cluster centers and are robust to outliers that might distort the true shape of clusters.

The correlation distance metric, d_c, is given by:

$$d_c(h,c) = 1 - \frac{(h-\bar{h})(c-\bar{c})'}{\sqrt{(h-\bar{h})(h-\bar{h})'}\sqrt{(c-\bar{c})(c-\bar{c})'}} \tag{4.9}$$

where overbars indicate averages and $(c-\bar{c})'$ indicates the transpose. Points that are well correlated have correlation distances that are close to zero, while points that are not well correlated have correlation distances close to 1.

The medoids and clusters are found through a series of optimization steps as follows:

1. k points are randomly assigned as medoids, c

2. the similarity metric, based on correlation distance or the mahalanobis distance, between the medoids, c, and all other points, h, is calculated and points are assigned to their closest medoid

3. the average similarity of each cluster is computed

4. the medoids and all other points are compared in pairs; if the average similarity score of the group is improved by swapping each c and h then the points are swapped

5. this iteration process is continued until an optimal group of points is chosen which minimizes the dissimilarity (equivalent to maximizing the similarity) score for all clusters

The features for clustering were selected based on a study of six calving events which indicated appropriate frequency bands to be studied as well as expected levels. The full list of features that will be used for clustering of the data, calculated for each minute of data, is as follows:

1. the average L_{10} levels for frequencies from 50 Hz to 100 Hz;

2. the average L_{10} levels for frequencies 1400 and 2500 Hz;

3. the average σ_T for frequencies from 50 Hz to 100 Hz;

4. the average σ_T for frequencies 1400 and 2500 Hz.

The scatterplot matrix for all features is shown in Figure 4.4. There appear to be two well-defined clusters in the plots of σ_T and the average L_{10} for the 50 to 100 Hz frequency bands, likely driven by the bimodality of the the average L_{10} levels for frequencies from 50 Hz to 100 Hz.

K-medoids clustering was implemented using the k-medoids function within MATLAB (Mathworks Inc.) set to use the original algorithm proposed by [22]; clustering was repeated 5 times, each with a new set of centroids before final assignments were made for the requested 3 clusters. The resultant clusters were inspected and compared with times identified by the WHOI team.

4.3 Results and Discussion

4.3.1 Lessons from PE Modeling and Inferred Calving Source Spectra

Six calving events were isolated and their spectra are shown in Figure 4.5; these spectra are the average of 10 one-second spectra and have been further smoothed with a 5 point moving average window. The events have been confirmed by checking for photographic evidence of a calving event at these times (to the nearest minute) and listening to the audio files. The background noise spectra for these time periods are also shown as dotted lines in the

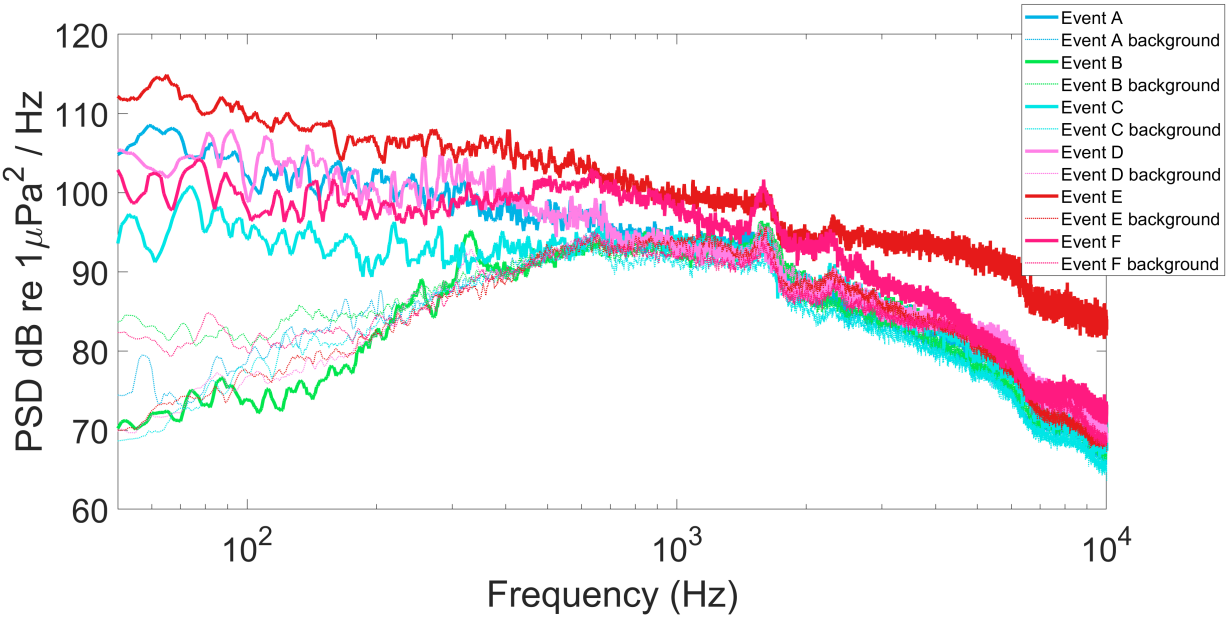

Figure 4.5: Spectra for six calving events are shown (solid lines) along with the background noise spectra within a minute of the event (dashed lines). The smallest event, Event B is approximately 6 dB above the background noise and was faintly audible in the recordings.

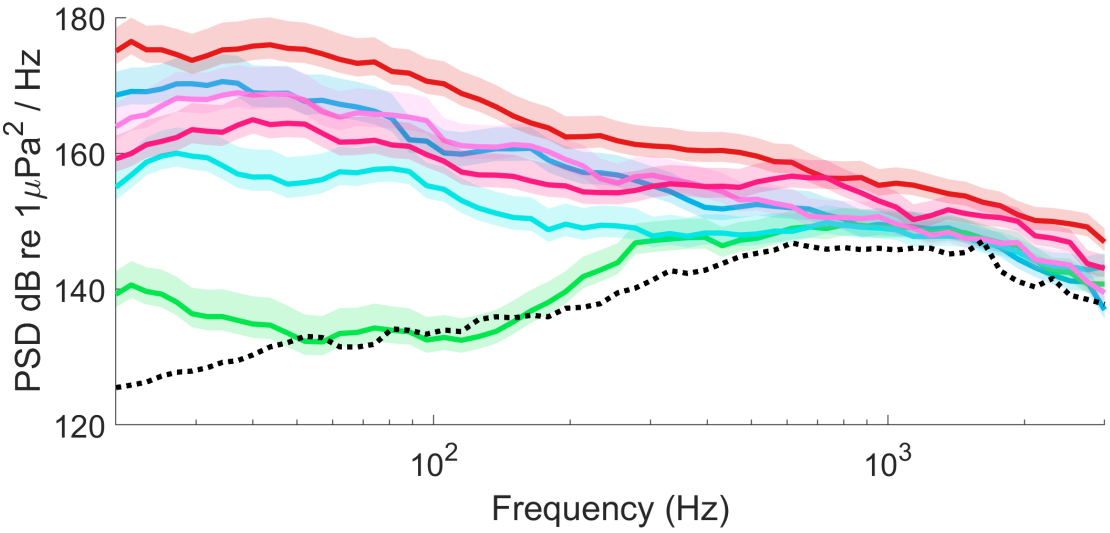

Figure 4.6: Spectra for six calving events are shown (solid lines) along with an estimate of the average background noise spectrum (dashed line). The bounds of the spectral estimates are indicated by the shaded region for each spectrum. The spectra follow a nominal 17 dB/decade trend. The color order from Figure 4.5 is maintained here.

figure; these are the average of 20 one-second spectra from time periods within a minute of the event. One of these events, Event B, is photographically-confirmed to be a small event and the remaining events are known to be large events. The spectral peak appears to be indicative of the size of the event and is nominally 6 dB above the background noise level.

All spectra were subsequently corrected for transmission loss using bounds derived as previously explained in Section 4.2.2 to estimate spectral levels that could be nominally expected at the calving face. We note that H_{av} was approximately 66 dB and 55 dB at 20 Hz and 1000 Hz, respectively. The corresponding upper and lower bounds, H_+ and H_-, were approximately 69 dB and 64 dB at 20 Hz and 58 dB and 54 dB at 1000 Hz, respectively. These corrected spectra are shown in Figure 4.6; solid lines indicate the estimated average spectral levels and the shaded regions indicate the bounds of the spectral estimates. An estimate of background noise levels is also shown (black dotted line). This estimate of background noise in Figure 4.6 was computed from the average difference between the spectra of the smallest event and background noise levels at the recorder location as a function of frequency - a background noise offset. This offset is maintained for the corrected spectra of the smallest event in Figure 4.6, so the notional background curve is the offset the same distance from the source spectrum of the smallest event as it is for the received spectrum of the smallest event.

4.3.2 Spectral Analysis: Empirical and Modeled Probability Density

The empirical probability densities of all frequency bands computed from the PSD can be visualized using a spectral probability density (SPD) plot as shown in Figure 4.7. The SPD gives the probability of observing a PSD for a given center frequency within the range of interest. If the background spectra in Figure 4.5 are compared with the areas of high probability density in Figure 4.7 (yellow regions) we see that the background noise spectrum can be inferred from the spectral probability density plot. The general shape of the background spectrum is captured here and appears to be bimodal, reflecting two common states within the dataset likely related to changes in the background noise environment over the course of

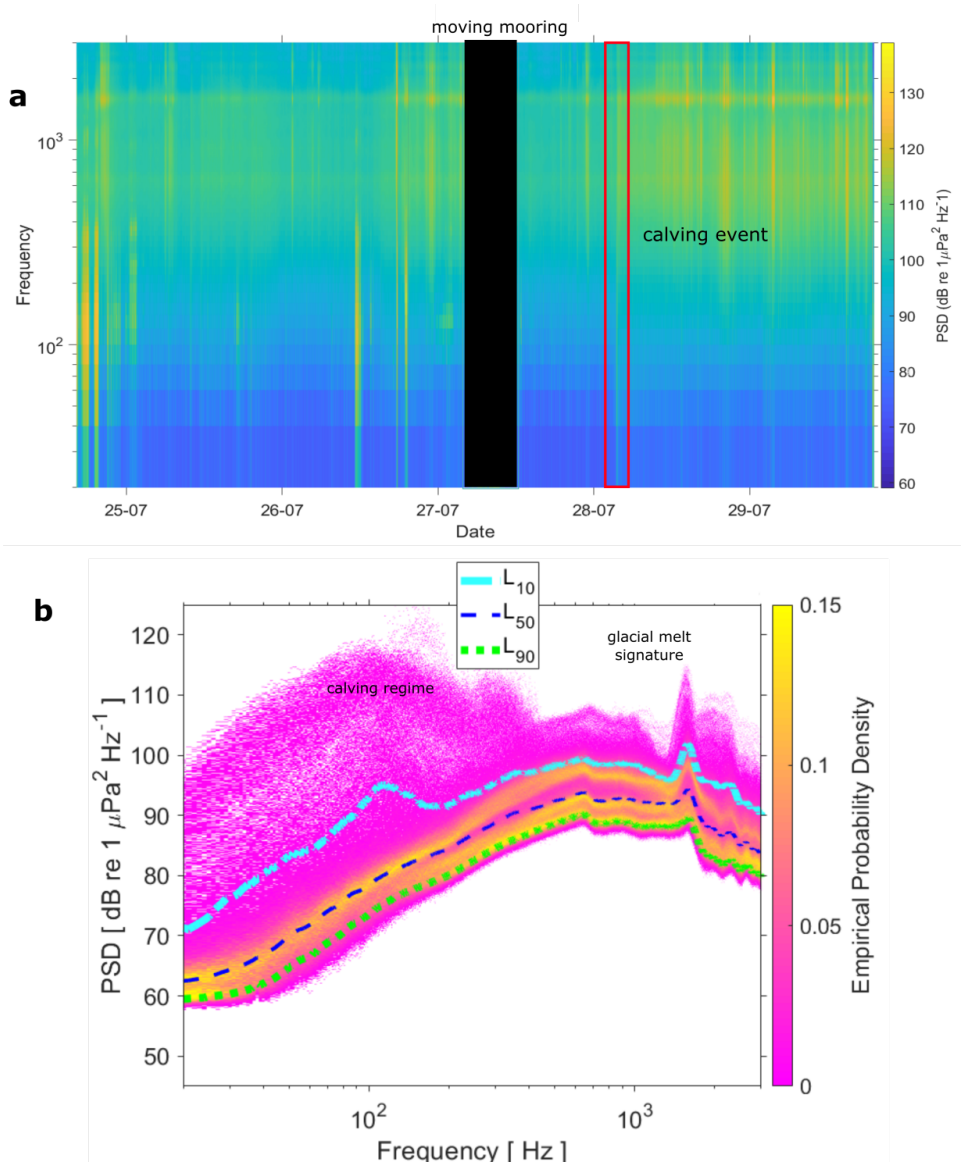

Figure 4.7: PSD summary of data. a. Spectrogram of noise measured in a West Greenland fjord represented for 5 days of data from July 25th 2013 to July 29th 2013 and b) spectral probability density plot for all data from the same time period. The PSD for every second of data was estimated using unwindowed data and no overlap. a. The spectrogram shows the calendar time series view of the PSD with a period believed to be associated with the movement of the mooring removed; broadband events (such as the red outlined event) are typically calving events within the dataset and the glacial melt signature can also be observed (purple outlined area). b. The characteristics of noise related to the glacial melt plume can be observed (annotated peak). The spectral probability density plot shows the most likely observed levels throughout the dataset combined with exceedance percentiles, L_x, to show the percentage of time that given PSD levels are exceeded. In this view the dominant background spectrum can be intuited based on the bright yellow band (the most often observed levels for a given frequency band). The broad magenta peak in the SPD indicates calving activity.

the deployment period.

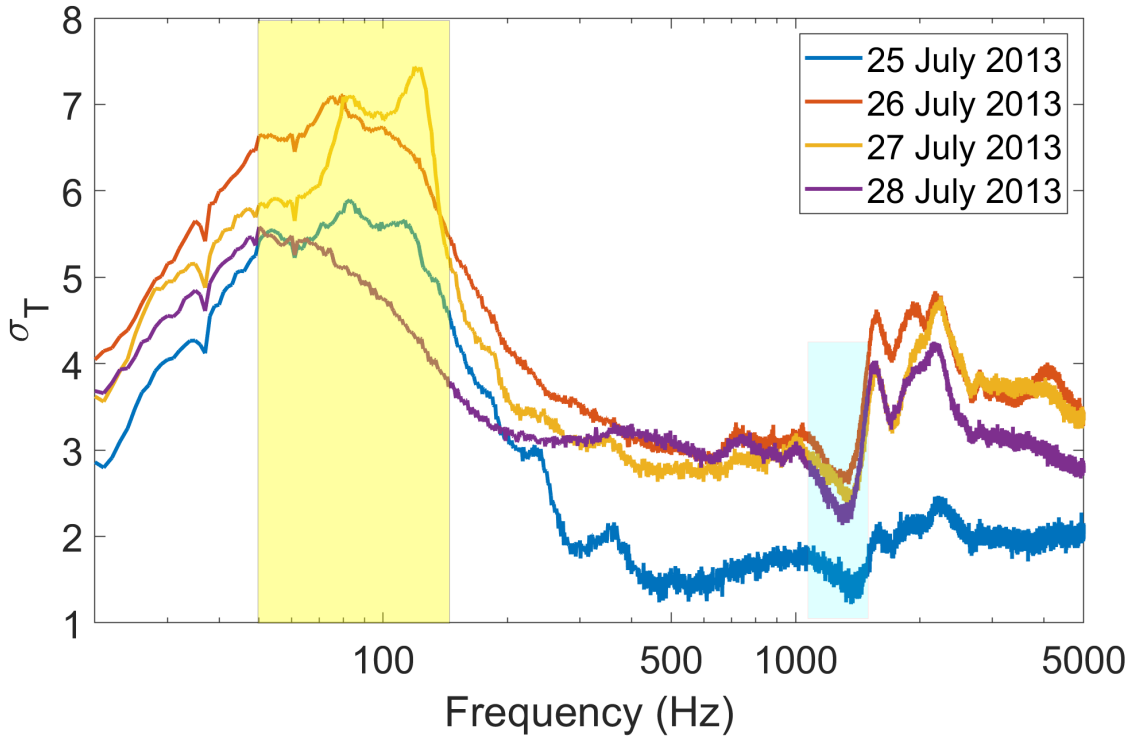

Figure 4.8: Daily σ_T for 25-28 July, 2013; σ_T (Eq. 4.7) equals $\sqrt{Var(s) - 5.57^2}$ where s is the dB equivalent of a single spectral estimate, $|X_f^2|$. Frequency bands with low values of σ_T (blue shaded region), such as the 1000 Hz and 1400 Hz frequency bands (within the band associated with glacial melt), could be expected to be reasonably well described by a random variable with a standard deviation of 5.57 dB. Frequency bands below 200 Hz (yellow shaded region), such as 50 Hz and 100 Hz are associated with calving activity, and their higher values of $\sigma_T$indicate the less steady nature of noise within these bands.

A daily summary of the σ_T as discussed in Section 4.2.3 in Equation 4.6, is shown in Figure 4.8. All days show consistent minima between 1000 and 1500 Hz (blue shaded region) and peaks observed between 30 and 150 Hz as well as between 1500 and 2500 Hz (yellow shaded regions). This trend can also be seen in the spread of the magenta areas (the minimum spread) of the SPD plot. A peak between 1000 and 1500 Hz in the SPD plot is present at all exceedance levels. We infer that this persistent feature is likely related to the glacial

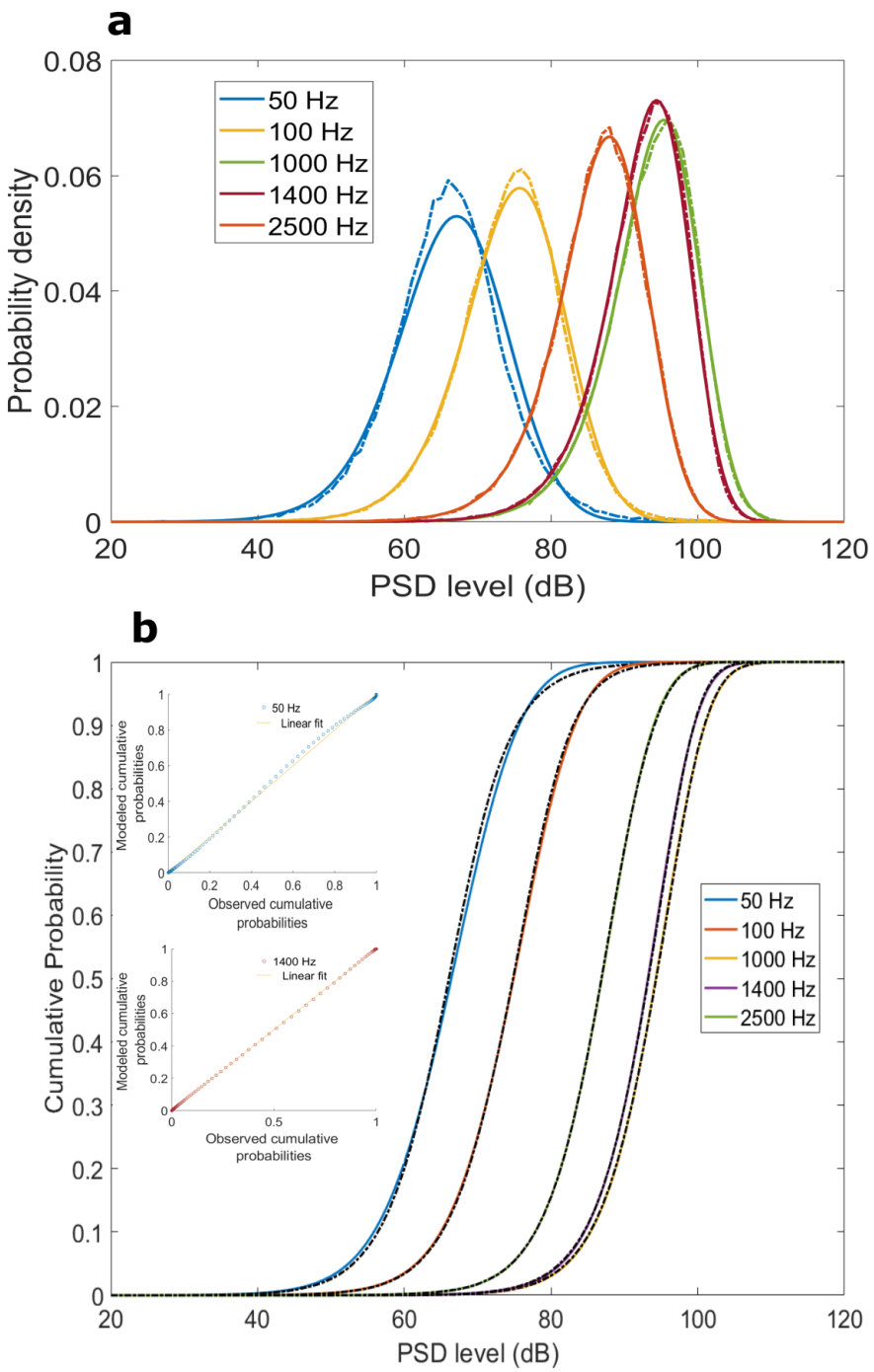

Figure 4.9: Comparison of modeled and empirical PDFs (a) and cumulative distribution functions (CDFs) (b) for July 28, 2013. Modeled PDFs are shown as solid lines and empirical PDFs are shown as dotted lines for frequencies 50, 100, 1000, 1400 and 2500 Hz. The inset plots in b indicate the linear fit of the modeled and empirical CDFs. The linear fit is better for higher frequencies, but the fit for the lower frequency bands is still acceptable.

melt signature observed by others [16,31] since a broad peak between 1000 and 3000 Hz was attributed to bubble release events.

As discussed in Section 4.2.3, σ_T can be used to model the PDFs for all frequency bands and therefore the empirical PDFs used to construct Figure 4.7 can be replaced by analytical PDFs. Figure 4.9 compares the empirical and modeled PDFs for 50, 100, 1000, 1400 and 2500 Hz. Different regimes are noted near the indicator frequencies for calving, 50 Hz and 100 Hz, and the melt signature, 1350 Hz. From the discussion in Section 4.2.3 we can infer that the spectral levels, s, for the 1000 Hz and 1400 Hz frequency bands can be well described by a RV with a standard deviation of 5.57 dB because of their low σ_T values. Although the modeled PDFs for 50 Hz and 100 Hz are not as well modeled - as expected by the higher σ_T values in Figure 4.8 for frequencies below 200 Hz, these bands are still sufficiently well-modeled (Figure 4.9b) to validate the applicability of Equation 4.4 in this case.

4.3.3 Detection of Events and Application of Unsupervised Classification

The clusters obtained using the correlation distance metric are shown in Figure 4.10 and Figure 4.11 as colored data points. The correlation distance metric roughly identifies three states within the dataset: nominally quiescent (cluster 1), periods of elevated noise levels likely associated with calving (cluster 3) and peak levels associated with calving (cluster 2).

Figure 4.10 and Figure 4.11 can be compared with the clusters obtained using the mahalanobis distance metric and shown in Figure 4.12 and Figure 4.13. Cluster 3 appears to be mostly localized to the time before the large calving event at approximately 04:00; clusters 1 and 2 are mixed and difficult to parse into calving and non-calving time periods, so are not useful for identifying calving time periods.

It is important to note that results from unsupervised clustering methods should be evaluated for the characteristics of the clusters they produce and the kinds of questions that might be answered from a particular method. For example, audio recordings of periods identified by the cluster 3 based on minimization of correlation distance are likely to be more useful for streamlining the labeling of times of audible calving events, however the

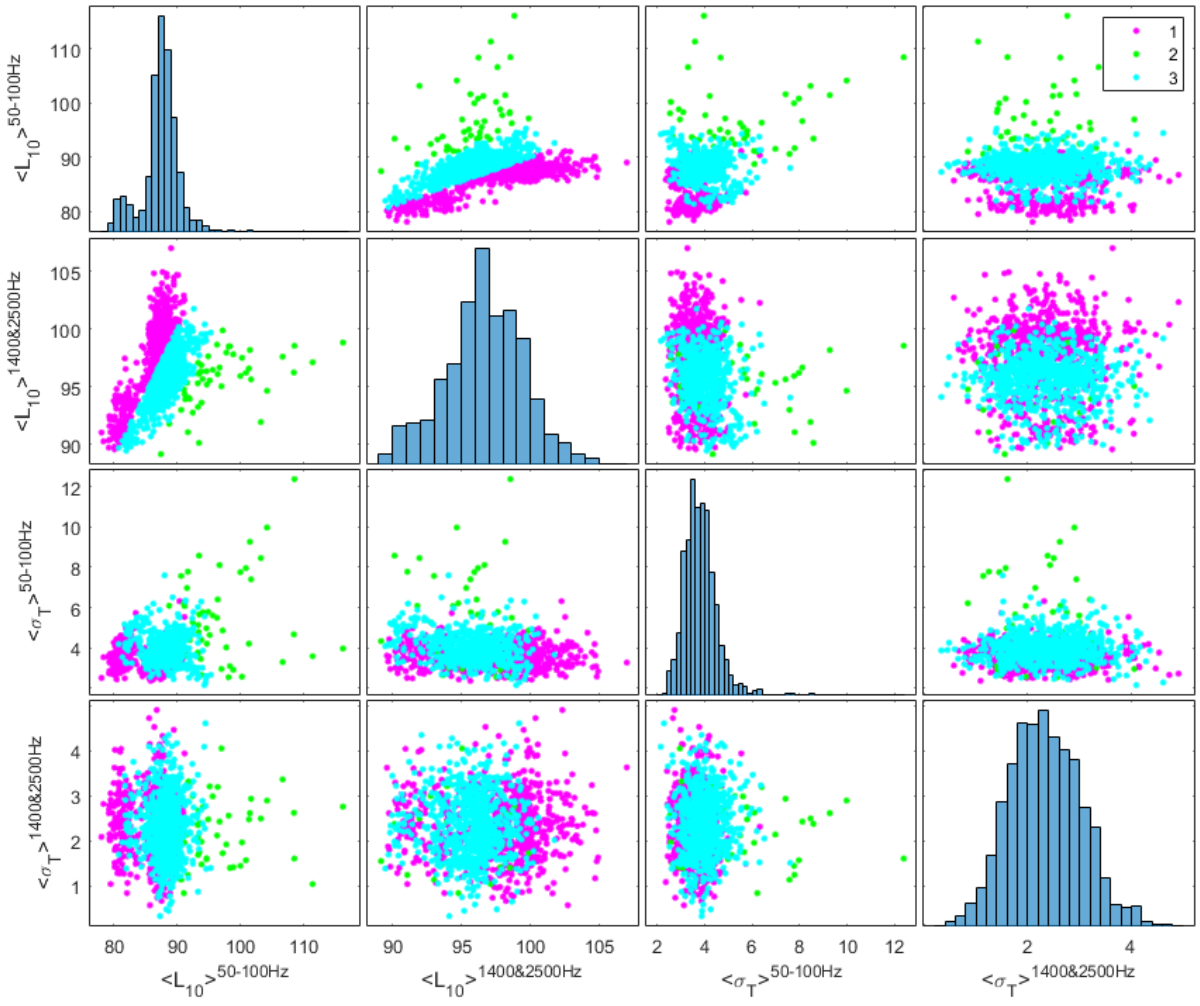

Figure 4.10: Scatter plot matrix showing relationships between paired combinations of clustered features first shown in Figure 4.4; the same data are being shown, but each of the 1440 points is colored according to its assigned cluster based on unsupervised clustering using the k-medoids algorithm. Points were assigned to clusters based on the correlation distance.This distance metric appears to roughly identify the clusters that can readily be observed by eye in Figure 4.4. Clusters 1 and 3 (magenta and cyan dots, respectively) appear to capture most of the two main clusters, while cluster 2 (green dots) appears to indicate outliers.

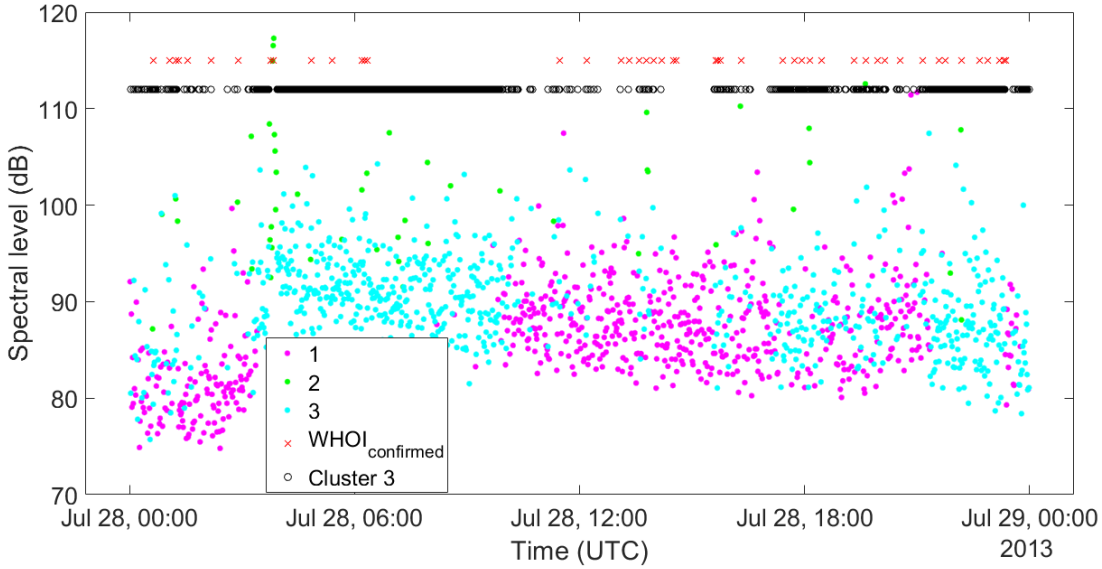

Figure 4.11: Time series plot of clustered features using the correlation distance metric. This distance metric identifies three states within the dataset: nominally quiescent (cluster 1, magenta dots), periods of elevated noise levels likely associated with calving (cluster 3, green dots) and peak levels associated with calving (cluster 2, cyan dots). The red crosses indicate times where events have been photographically confirmed by the WHOI team. These are compared with times from cluster 3 (black circles).

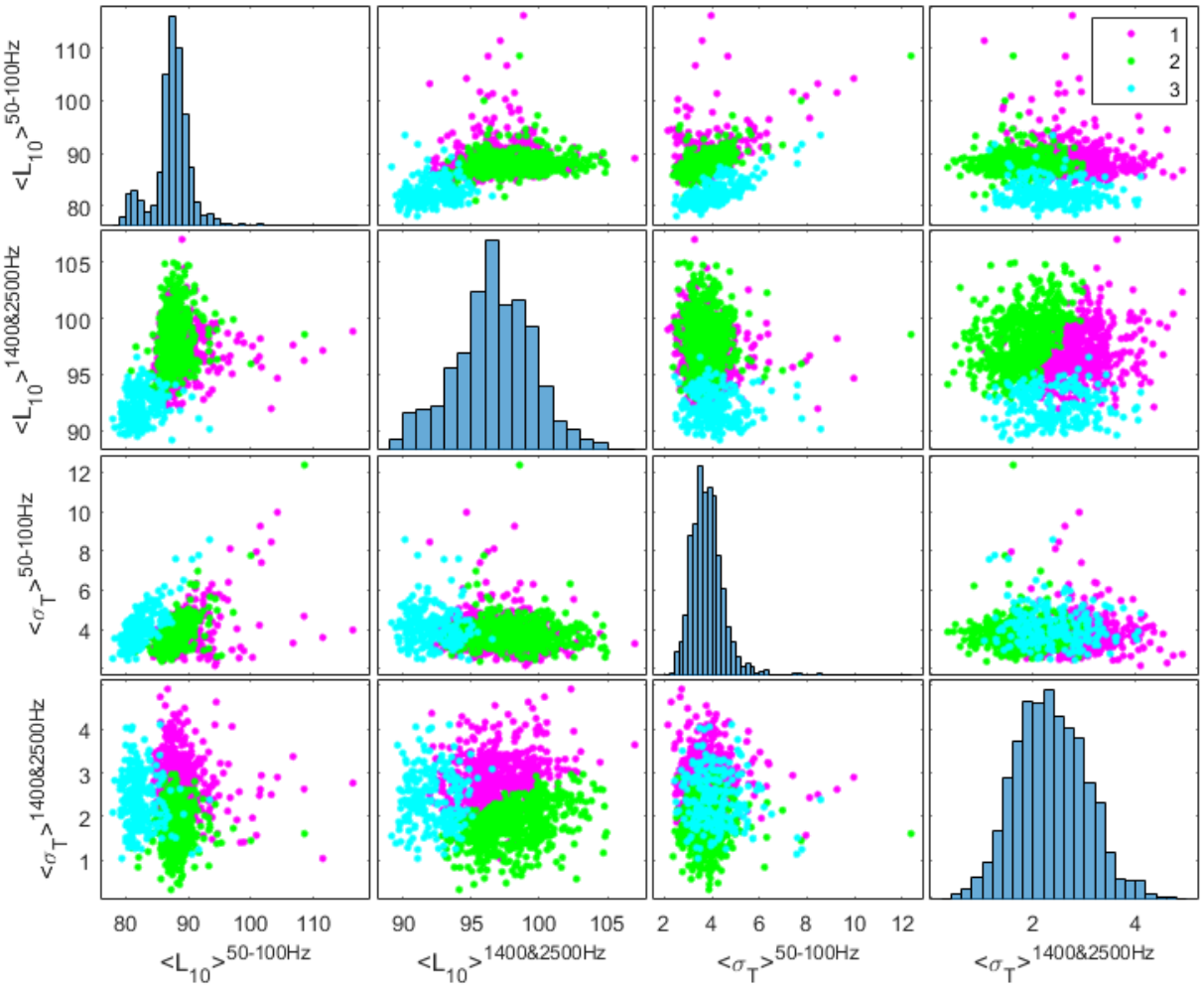

Figure 4.12: Scatter plot matrix showing relationships between paired combinations of clustered features first shown in Figure 4.4; the same data are being shown, but each of the 1440 points is colored according to its assigned cluster based on unsupervised clustering using the k-medoids algorithm. Points were assigned to clusters based on the mahalanobis distance metric. Clusters 2 and 3 (green and cyan dots, respectively) are not as well separated as in Figure 4.10. Cluster 3 (cyan dots) appears to be mostly restricted to low L_{10} levels.

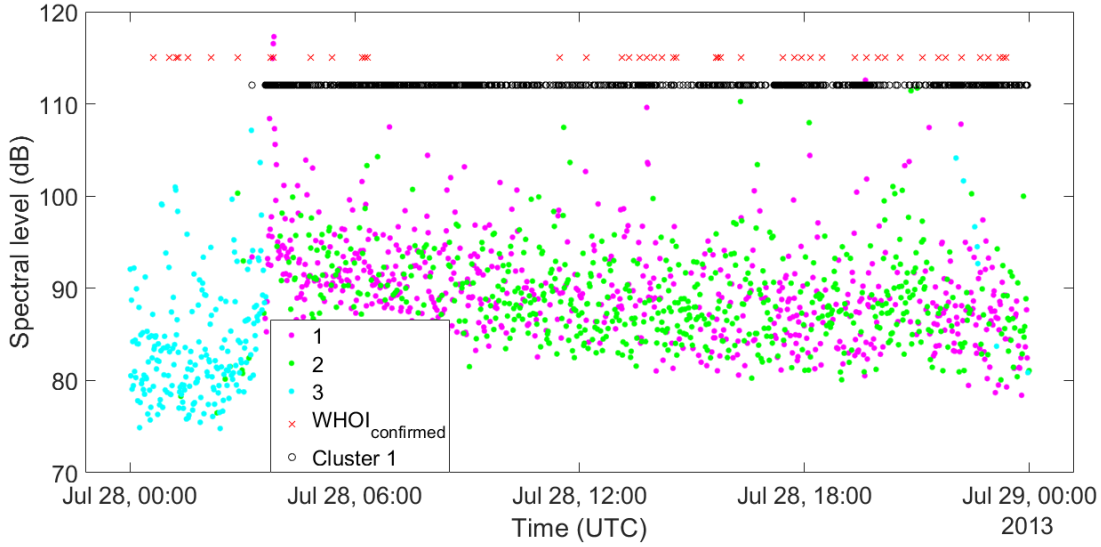

Figure 4.13: Time series plot of clustered features using the mahalanobis distance metric. Clusters 1 (magenta dots) and 2 (green dots) are not as well separated as in Figure 4.11. Cluster 3 (cyan dots) appears to be mostly limited to the time period before a large calving event at 04:00; noise levels did not return to this pre-event level. As in Figure 4.11, the red crosses indicate times where events have been photographically confirmed by the WHOI team. These can be compared with times from cluster 1 (black circles). This cluster does not appear to be as successful in identifying a distinct state.

cluster 3 based on minimization of mahalanobis distance might be useful for identifying long time periods where noise levels are the lowest within the dataset. The choice of method and distance metric and feature set may produce different clusters that may be useful for answering other questions about the dataset.

4.4 Summary and Additional Remarks

This paper discussed results from a study of underwater noise measured in a glacial fjord in West Greenland using an underwater recorder moored 11 m below the surface; the water depth at the mooring location was approximately 125 m. This underwater dataset [10] contains several examples of calving events.

Although this work does not encompass all the physics associated with the underwater sound associated with calving in a glacial fjord, it does illustrate the utility of the spectral probability density in evaluating background noise characteristics in the frequency domain, the utility of σ_T in quantifying the character of noise in frequency bands of interest, and the utility of k-medoids clustering as a pre-sorting method to inform the decision-making process on the selection of features on which to base the training of more complex algorithms.

The key points emerging from this work can be summarized as follows:

1. Glacier calving noise was studied using spectral probability density (SPD) which indicated levels suitable for the detection of calving events, and confirmed the presence of a signature related to glacial melt that has been observed by others [17, 23].

2. Six calving events were isolated and their spectral estimates were corrected for propagation loss within the fjord to provide nominal estimates of source spectral levels. A nominal 17 dB/decade trend was observed for the source spectra.

3. The spectral estimates $|X_f|^2$ used to study SPD, were exponentially distributed random variables, therefore the PDF of s, $10\log_{10}(|X_f|^2)$, could be modeled following an approach by [12] to obtain fits to the empirical data based on the method of moments.

4. These modeled PDFs were used to derive a parameter σ_T that might be thought of as indicating the steadiness of the character of noise within a particular frequency band. This parameter, σ_T, was calculated on two different time scales, 24 hours and 1 minute, and was used to study bands indicative of calving.

5. K-medoids clustering was utilized to cluster four features calculated every minute for 24 hours of data to identify periods that were indicative of calving events. Results from the clustering exploration were helpful in identifying time periods associated with calving noise.

Future work may explore the performance of more advanced machine learning techniques, such as long short-term memory (LSTM) networks, using the most promising features identified from the clustering exploration undertaken here.

Chapter 5

CONCLUDING REMARKS

This dissertation presents a compilation of my exploration of various methods related to mapping, metrics and modeling useful in the study of acoustic data. Special emphasis has been placed on the exploration of data from a Greenland fjord and some of these methods were also initially explored using the TREX dataset.

The key points emerging from this work can be summarized as follows:

1. In the analysis of the TREX dataset, SPD was useful in exploring daily and overall trends within three frequency bands were explored within. The L_{50} was 60 dB re 1 μ Pa^2/Hz for both the 1800 to 3600 Hz frequency band as well as a frequency band centered at 3.5 kHz of 100 Hz bandwidth averaged over day and night.

2. Contributions to the background level from suspected biological sources were investigated and the frequency range of one of the diurnal biological signals makes it significant to the analysis of TREX13 experimental signals since it is within the 1 to 10 kHz frequency band in which signals were broadcast and is consistently present after dusk and before dawn.

3. In the analysis of the TREX dataset, an approximate 10 dB difference in peak levels was observed between the end and onset of astronomical twilight with the lowest levels observed immediately after dawn. The data suggest that the lowest noise levels are constrained by wind above a threshold in the absence of biological and anthropogenic masking noise.

4. Glacier calving noise was studied using spectral probability density (SPD) which indi-

cated levels suitable for the detection of calving events, and confirmed the presence of a signature related to glacial melt that has been observed by others [17, 23].

5. Six calving events were isolated and their spectral estimates were corrected for propagation loss within the fjord to provide nominal estimates of source spectral levels. This is applicable as part of a growing body of observations of calving events leading to source models of calving events. A nominal 17 dB/decade trend was observed for the source spectra.

6. The spectral estimates $|X_f|^2$ used to study SPD, were exponentially distributed random variables, therefore the PDF of s, $10\log_{10}(|X_f|^2)$, could be modeled following an approach by [12] to obtain fits to the empirical data based on the method of moments.

7. These modeled PDFs were used to derive a parameter σ_T that might be thought of as indicating the steadiness of the character of noise within a particular frequency band. This parameter, σ_T, was calculated on two different time scales, 24 hours and 1 minute, and was used to study bands indicative of calving.

8. K-medoids clustering was utilized to cluster four features calculated every minute for 24 hours of data to identify periods that were indicative of calving events. Results from the clustering exploration were helpful in identifying time periods associated with calving noise. Clustering was also utilized in the exploration of the TREX dataset. A time series view of the clusters the three clusters again seemed to indicated different states within the dataset; one cluster was primarily associated with quiet periods when wind noise dominated the lowest levels, while another was likely indicative of a mixture of processes influencing levels and the third was restricted to high amplitude events. Inspection of long-term spectrograms and listening to recordings from these periods was used to postulate the source of these events.

The methods employed here are broadly applicable to other underwater noise datasets.

Future work with the Greenland dataset may explore the performance of more advanced machine learning techniques, using the most promising features identified from the clustering exploration undertaken here and other features yet to be discovered.

A synergistic application of mapping, metrics and modeling (both statistical and acoustic) could be anticipated to be useful in a study of underwater noise, resulting in a reduction of labor and monitoring costs and a broader utility in the resultant modeling products.

BIBLIOGRAPHY

[1] C.J. Amante, M.R. Love, L.A. Taylor, and B.W. Eakins. *Digital Elevation Model of Panama City, Florida: Procedures, Data Sources and Analysis*. NOAA technical memorandum NESDIS NGDC-50. U.S. Department of Commerce, National Oceanic and Atmospheric Administration, National Environmental Satellite, Data, and Information Service, National Geophysical Data Center, Marine Geology and Geophysics Division, 2011.

[2] Douglas I. Benn, Charles R. Warren, and Ruth H. Mottram. Calving processes and the dynamics of calving glaciers. *Earth-Science Reviews*, 82(3):143–179, 2007.

[3] David MF Chapman. A simple estimate of propagation loss fluctuations due to modal interference. *The Journal of the Acoustical Society of America*, 85(3):1097–1106, 1989.

[4] Chen-Tung Chen and Frank J Millero. Speed of sound in seawater at high pressures. *The Journal of the Acoustical Society of America*, 62(5):1129–1135, 1977.

[5] Barbara Christian deMoustier. The authors thank Christian de Moustier and Barbara Kraft for processing and sharing their survey results, 2013.

[6] Michael D Collins. A split-step padé solution for the parabolic equation method. *The Journal of the Acoustical Society of America*, 93(4):1736–1742, 1993.

[7] Martin A Connaughton. Sound generation in the sea robin (prionotus carolinus), a fish with alternate sonic muscle contraction. *Journal of Experimental Biology*, 207(10):1643–1654, 2004.

[8] L. Coquereau, J. Grall, and L. Chauvaud. Sound production and associated behaviours of benthic invertebrates from a coastal habitat in the north-east atlantic. *Mar Biol*, 163(127):173–185, 2016.

[9] GB Crocker. Size distributions of bergy bits and growlers calved from deteriorating icebergs. *Cold regions science and technology*, 22(1):113–119, 1993.

[10] P Dahl. Greenland fjord passive acoustic data, Saqardleq fjord, West Greenland, 2013, 2017.

[11] Peter H Dahl and David R Dall'Osto. On the underwater sound field from impact pile driving: Arrival structure, precursor arrivals, and energy streamlines. *The Journal of the Acoustical Society of America*, 142(2):1141–1155, 2017.

[12] Peter H Dahl and William J Plant. The variability of high-frequency acoustic backscatter from the region near the sea surface. *The Journal of the Acoustical Society of America*, 101(5):2596–2602, 1997.

[13] Vincent A Del Grosso. New equation for the speed of sound in natural waters (with comparisons to other equations). *The Journal of the Acoustical Society of America*, 56(4):1084–1091, 1974.

[14] Dara M Farrell, David R DallOsto, and Peter H Dahl. The background noise environment during the 2013 target and reverberation experiment. *IEEE Journal of Oceanic Engineering*, 42(4):1088–1093, 2017.

[15] GJ Franz. Splashes as sources of sound in liquids. *The Journal of the Acoustical Society of America*, 31(8):1080–1096, 1959.

[16] Oskar Glowacki, Grant B Deane, and Mateusz Moskalik. The intensity, directionality, and statistics of underwater noise from melting icebergs. *Geophysical Research Letters*, 45(9):4105–4113, 2018.

[17] Oskar Glowacki, Mateusz Moskalik, and Grant B. Deane. The impact of glacier meltwater on the underwater noise field in a glacial bay. *Journal of Geophysical Research: Oceans*, 2016.

[18] Michele B Halvorsen, Brandon M Casper, Frazer Matthews, Thomas J Carlson, and Arthur N Popper. Effects of exposure to pile-driving sounds on the lake sturgeon, nile tilapia and hogchoker. *Proceedings of the Royal Society B: Biological Sciences*, 279(1748):4705–4714, 2012.

[19] C. Hennig, M. Meila, F. Murtagh, and R. Rocci. *Handbook of Cluster Analysis*. Chapman & Hall/CRC Handbooks of Modern Statistical Methods. CRC Press, 2015.

[20] S.A. Hsu, Ericm A. Meindl, and David B. Gilhousen. Determining the power-law wind-profile exponent under near-neutral stability conditions at sea. *Applied Meterology*, 33(6), 1994.

[21] Finn B Jensen, William A Kuperman, Michael B Porter, and Henrik Schmidt. *Computational ocean acoustics*. Springer Science & Business Media, 2011.

[22] Leonard Kaufman and Peter J Rousseeuw. *Finding groups in data: an introduction to cluster analysis*, volume 344. John Wiley & Sons, 2009.

[23] Kevin M Lee, Preston S Wilson, and Erin C Pettit. Underwater sound radiated by bubbles released by melting glacier ice. In *Proceedings of Meetings on Acoustics 166ASA*, volume 20,1, page 070004. ASA, 2013.

[24] Tristan Lippert, Michael A Ainslie, and Otto von Estorff. Pile driving acoustics made simple: Damped cylindrical spreading model. *The Journal of the Acoustical Society of America*, 143(1):310–317, 2018.

[25] Delphine Mathias, Cédric Gervaise, and Lucia Di Iorio. Wind dependence of ambient noise in a biologically rich coastal area. *The Journal of the Acoustical Society of America*, 139(2):839–850, 2016.

[26] Nathan D Merchant, Tim R Barton, Paul M Thompson, Enrico Pirotta, D Tom Dakin, and John Dorocicz. Spectral probability density as a tool for ambient noise analysis. *The Journal of the Acoustical Society of America*, 133(4):EL262–EL267, 2013.

[27] Shree S Nath, John P Bolte, Lindsay G Ross, and Jose Aguilar-Manjarrez. Applications of geographical information systems (gis) for spatial decision support in aquaculture. *Aquacultural Engineering*, 23(1-3):233–278, 2000.

[28] Jeffrey A Nystuen. Quantifying physical processes in the marine environment using underwater sound. *Proceedings of the 4th International Conference and exhibition on Underwater acoustic measurements: technologies & results*, pages 1171–1178, 2011.

[29] Leipnik M. R Yoon J Padmanabhan, G. A glossary of GIS terminology (92-13). *UC Santa Barbara: National Center for Geographic Information and Analysis. NCGIA Technical Reports*, 1992.

[30] Donald B Percival. *Spectral analysis for physical applications : multitaper and conventional univariate techniques*. Cambridge University Press, 1993.

[31] Erin Christine Pettit, Kevin Michael Lee, Joel Palmer Brann, Jeffrey Aaron Nystuen, Preston Scot Wilson, and Shad O'Neel. Unusually loud ambient noise in tidewater glacier fjords: A signal of ice melt. *Geophysical Research Letters*, 42(7):2309–2316, 2015.

[32] C.L. Piggott. Ambient sea noise at low frequencies in shallow water of the scotian shelf. *The Journal of the Acoustical Society of America*, 36:2152, 1965.

[33] Arthur N Popper and Mardi C Hastings. The effects of human-generated sound on fish. *Integrative Zoology*, 4(1):43–52, 2009.

[34] Peter J Rousseeuw. Silhouettes: a graphical aid to the interpretation and validation of cluster analysis. *Journal of computational and applied mathematics*, 20:53–65, 1987.

[35] MC Sanjana, G Latha, A Thirunavukkarasu, and R Venkatesan. Ambient noise field and propagation in an arctic fjord kongsfjorden, svalbard. *Polar Science*, 17:40–49, 2018.

[36] T. Stanton. Summary of fish observations during TREX2013. Unpublished.

[37] T. Stanton. private communication, 2016.

[38] Laura A Stevens, Fiamma Straneo, Sarah B Das, Albert J Plueddemann, Amy L Kukulya, and Mathieu Morlighem. Linking glacially modified waters to catchment-scale subglacial discharge using autonomous underwater vehicle observations. *The Cryosphere*, 10:417–432, 2016.

[39] RJ Urick. *Principles of Underwater Sound for Engineers*. McGraw-Hill, Inc., 1976.

[40] "USGS". *usSEABED: Gulf of Mexico and Caribbean (Puerto Rico and US Virgin Islands) offshore surficial-sediment data release*. [Online; accessed 20-June-2019].

[41] Till JW Wagner, Fiamma Straneo, Clark G Richards, Donald A Slater, Laura A Stevens, Sarah B Das, and Hanumant Singh. Large spatial variations in the flux balance along the front of a greenland tidewater glacier. *The Cryosphere*, 13(3):911–925, 2019.

[42] C. Wall and D. Mann. private communication, 2016.

[43] Carrie C. Wall, Peter Simard, Chad Lembke, and David A. Mann. Large-scale passive acoustic monitoring of fish sound production on the West Florida Shelf. *Marine Ecology Progress Series*, 484:173, June 2013.

[44] Peter C Wille and Detlef Geyer. Measurements on the origin of the wind-dependent ambient noise variability in shallow water. *NOAA Technical Memorandum NESDIS NGDC-50*, 75(1):173–185, 1984.

[45] ZY Zhang and CT Tindle. Improved equivalent fluid approximations for a low shear speed ocean bottom. *The Journal of the Acoustical Society of America*, 98(6):3391–3396, 1995.

[46] Dapeng Zou, Kevin L Williams, and Eric I Thorsos. Influence of temperature on acoustic sound speed and attenuation of seafloor sand sediment. *IEEE Journal of Oceanic Engineering*, 40(4):969–980, 2014.